Journal of the Brazilian Society of Mechanical Sciences and Engineering (2022) 44:531
https://doi.org/10.1007/s40430-022-03829-9

TECHNICAL PAPER

A unified formulation for composite quasi-3D elements based on global–local superposition. Part II: Implementation and numerical assessment

Alfredo R. de Faria[1]

Received: 30 December 2021 / Accepted: 27 September 2022 / Published online: 17 October 2022

Abstract
This two-paper series proposes a unified theory that gives rise to a family of quasi-3D composite elements. The first paper presents the element formulation and its basic capabilities: the ability to capture transverse normal (σ_z) and shear (τ_{yz}, τ_{xz}) stresses, suitability for thermoelastic analyses and compliance to both displacements and transverse stress continuity requirements. These capabilities are inherent to the element since a global–local superposition approach is devised that, from inception, guarantees that equilibrium equations, continuity consistency and boundary conditions are fully met. A simple validation analysis was conducted in part I that initially pointed to a very promising direction with high numerical efficiency of the element. This second paper investigates the element numerical performance under different scenarios: use of three- and four-node parent elements, degree of global interpolation functions, adequacy of different local interpolation functions (F_0, F_1, G_0, G_1, H_0, H_1) and consideration of a more practical configuration of a reinforced panel consisting of multiple laminates. Through-the-thickness displacements, strains and stresses are obtained and shown to be of reasonable accuracy. Results are compared against a highly refined mesh of 3D brick elements implemented in a commercial software that provide a benchmark for the elements capabilities.

Keywords Finite element · Composite plate · Through-the-thickness effects · Zigzag

1 Introduction

Structural components such as plates and shells are largely used in civil, mechanical and aerospace industries. When subjected to transverse loads, they develop through-the-thickness shear and normal strains. These strains are not well described or captured by classical theories commonly employed in the formulation of elements based on pure displacement and rotation interpolation. Unfortunately, most refinements of classical element formulations either are redundant or provide only marginal incremental enhancements, unless transverse stress continuity requirements between layers are imposed. However, in many theories, and consequently in existing higher-order beam and plate finite element formulations, no consideration is made regarding normal stress and strain effects ($\varepsilon_z \neq 0$) on the bending, buckling and vibration responses when these theories are applied to both monolithic and sandwich laminates. One of the most widespread classical theories is the equivalent single-layer theories [1]. Due to their simplicity, equivalent single-layer theories are popularly employed in the bending, free vibration and buckling analyses of laminated beams and plates. However, these theories are incapable of capturing accurate structural responses in sandwich laminates. Zigzag theories [2, 3], or layerwise displacement field theories, are more accurate, especially in the analysis of sandwich laminates with soft cores. The inherent difficulty with the zigzag theories is, usually, the large number of unknowns that must be treated as degrees of freedom. The newly proposed theory in part I offers a formulation with the same capabilities as the zigzag theory, but with a reduced (and fixed) number of degrees of freedom, independent of the number of layers in the laminate.

Technical Editor: Flávio Silvestre.

✉ Alfredo R. de Faria
arfaria@ita.br

[1] Department of Mechanical Engineering, Instituto Tecnológico de Aeronáutica (ITA), Praça Marechal Eduardo Gomes, 50, São José dos Campos, SP 12228-900, Brazil

The proposed theory can be used in the formulation of new elements applicable to bending, vibration and buckling analyses of both monolithic and sandwich laminates. Initially, elements designed to work under linear regime must be developed, followed by elements able to perform linearized buckling analyses (geometric stiffness matrix) and vibration (mass matrix). It is observed that the new elements are sufficiently accurate and efficient such that they avoid the need to use tridimensional finite element models in situations where the transverse stresses and strains are desired. The avoidance of tridimensional models is of particular relevance in lightweight designs, particularly in aerospace and automotive applications, where thin panels are required. The thinness of such panels naturally leads to tridimensional models with either hundreds of thousands of nodes, if aspect ratio is to be maintained close to 1.0, or to models with highly distorted 3D elements, what compromises accuracy. Moreover, it comes to iterative or nonlinear analyses, and tridimensional models are extremely computer-intensive, requiring hours or even days of simulations. The influence of the temperature profiles (heat conduction problem) on the thermoelastic response of multilayered laminates by the use of more elaborate theories with through-the-thickness capabilities is also assessed. The present paper includes thermoelastic effects in the element formulation, enabling them for analyses where temperature effects are relevant.

One practical example of the application of tridimensional models is crack propagation induced by delamination. Typically, in these cases, a combination of tridimensional modeling, to represent laminae of the laminate, and decohesive elements, to represent interfaces between laminae where cracks originate, is used. A potential application of the new formulation is to replace these complex models by elements with through-the-thickness capabilities that possess features that capture crack opening and propagation. For this purpose, it will be necessary to modify Eqs. (2–4) in part I to allow for discontinuities in the displacement fields u, v and w.

In the accompanying paper part I, a simple four-element validation under uniaxial stress (σ_z) showed promising results. However, no thorough investigations of the elements capabilities were conducted in order to assess its possible limitations, numerical accuracy and stability. Hence, the major objective of this paper part II is to critically assess these aspects and make recommendations toward more practical implementations of the element.

Global and local interpolation functions of increasing order are evaluated (linear, quadratic and cubic). In principle, non-polynomial interpolation functions can be used but the study is restricted to polynomials since they are by far the most commonly used in commercial finite element software. Single and multiple laminate configurations are considered. The ability to model reinforced laminates must not be discounted, disregarded or belittled since reinforced composite panels are one of the most frequently structural components encountered in real applications.

2 Interpolation functions and constitutive relations

In part I, the initial description of the element formulation was given assuming that Lagrange global interpolation functions would be used. This particular approach was adopted simply because it is didactically easier and more intuitive to explain the main features of the element in terms of Lagrange polynomials. Figure 4 in part I shows different "levels" of nodal planes (three levels for the tria and four levels for the quad) and it is more natural to explain the interpolation scheme proposed with the visual aid provided by Fig. 4. However, as reported in part I, a practical weakness of the element is that it cannot represent piecewise variable thickness or drop-off laminates if Lagrange polynomials are chosen as global interpolation functions. The way around this adversity was the use of monomials as global interpolation functions, where the respective coefficients related to each monomial correspond to a global nodal degree of freedom defined on the element mid-plane. Since, theoretically, there is no difference in choosing Lagrange polynomials or monomials (they are linearly dependent on one another), the latter is adopted because the monomials are the device that allow consideration of multiple laminate configurations.

When it comes to the local interpolation functions three possibilities are contemplated: ζ_k, ${\zeta_k}^2$ and ${\zeta_k}^3$. The constant coefficient local interpolation function is neglected by virtue of a numerical determent. Notice that the local functions firstly presented in Eqs. (2–4) of part I appear in pairs: F_0/F_1 for ${u_L}^{(k)}$, G_0/G_1 for ${v_L}^{(k)}$ and H_0/H_1 for ${w_L}^{(k)}$. In the case of ${w_L}^{(k)}$, if one assumes $H_0=1$ and H_1 is either ζ_k, ${\zeta_k}^2$ or ${\zeta_k}^3$, then matrix $\hat{\mathbf{Q}}_{33}$ in Eq. (72) of part I becomes singular due to enforcement of the displacement continuity condition in Eq. (9). Evidently this singularity deadly cripples the algorithm since matrix $\hat{\mathbf{Q}}_{33}$ must be invertible in order to eliminate the local degrees of freedom $\mathbf{w}^{(k)}$. The same holds with regard to F_0/F_1, matrix $\hat{\mathbf{Q}}_{44}$ and $\mathbf{u}^{(k)}$, and also with regard to G_0/G_1, matrix $\hat{\mathbf{Q}}_{55}$ and $\mathbf{v}^{(k)}$. More generally, the conditions for these matrices to be invertible are that there must be an even-order term in the local function (1 or ${\zeta_k}^2$) with nonzero first derivative with respect to ζ_k. However, the combination $H_0=1$ and $H_1={\zeta_k}^2$ is still unacceptable because the term H_1 has derivatives at bottom and top layer surfaces that obey $dH_1/d\zeta_k(-1)=-dH_1/d\zeta_k(+1)$, and since $dH_0/d\zeta_k=0$, it is easy to see that one can make one row of matrix $\hat{\mathbf{Q}}_{33}$ identically zero. The conclusion is that the constant coefficient local interpolation function is not viable.

The in-plane interpolation of ${u_G}^{(k)}$, ${v_G}^{(k)}$ and ${w_G}^{(k)}$ are fixed. However, the transverse global interpolation for ${u_G}^{(k)}$, ${v_G}^{(k)}$ and ${w_G}^{(k)}$ and the local interpolation for ${u_L}^{(k)}$, ${v_L}^{(k)}$ and ${w_L}^{(k)}$ can be selected to form a family of elements. Table 1 shows the combinations of global/local interpolations used to build six elements labeled A to F. The global interpolations must be the same for ${u_G}^{(k)}$, ${v_G}^{(k)}$ and ${w_G}^{(k)}$, whereas the local interpolations for ${u_L}^{(k)}$, ${v_L}^{(k)}$ and ${w_L}^{(k)}$ are independent, i.e., they can be different for ${u_L}^{(k)}$, ${v_L}^{(k)}$ or ${w_L}^{(k)}$. Even so, the local interpolations selected for the six types of elements were the same in order to simplify the assessment and reduce the number of combinations. Elements A, C and E contain linear and quadratic monomials that Liu and Li [4] called 1–2 superposition theory (ST). Elements B, D and F contain quadratic and cubic monomials, called 2–3 superposition theory (ST).

The choice of the interpolation functions has direct repercussions on the numerical efficiency of the element. Equation (1) shows the expression for the first variation of the element strain energy, where the terms contained therein were defined in the part I of this study. The integrals in Eq. (1) are numerically computed using Gaussian quadrature in the case of quadrilateral elements and similar integration schemes adapted for the case of triangular elements.

$$\delta U_e = \delta \mathbf{q}_e^T \int_A \sum_{k=0}^{n-1} \int_{z_k}^{z_{k+1}} \begin{Bmatrix} \mathbf{B}_{u,x}^{(k)T} \\ \mathbf{B}_{v,y}^{(k)T} \\ \mathbf{B}_{w,z}^{(k)T} \\ \mathbf{B}_{v,z}^{(k)T} + \mathbf{B}_{w,y}^{(k)T} \\ \mathbf{B}_{u,z}^{(k)T} + \mathbf{B}_{w,x}^{(k)T} \\ \mathbf{B}_{u,y}^{(k)T} + \mathbf{B}_{v,x}^{(k)T} \end{Bmatrix}^T \mathbf{C}^{(k)} \left(\begin{Bmatrix} \mathbf{B}_{u,x}^{(k)} \\ \mathbf{B}_{v,y}^{(k)} \\ \mathbf{B}_{w,z}^{(k)} \\ \mathbf{B}_{v,z}^{(k)} + \mathbf{B}_{w,y}^{(k)} \\ \mathbf{B}_{u,z}^{(k)} + \mathbf{B}_{w,x}^{(k)} \\ \mathbf{B}_{u,y}^{(k)} + \mathbf{B}_{v,x}^{(k)T} \end{Bmatrix} \mathbf{q}_e + \begin{Bmatrix} 0 \\ 0 \\ a_{w,z}^{(k)} \\ a_{v,z}^{(k)} \\ a_{u,z}^{(k)} \\ 0 \end{Bmatrix} - \Delta T \begin{Bmatrix} \alpha_x^{(k)} \\ \alpha_y^{(k)} \\ \alpha_z^{(k)} \\ 0 \\ 0 \\ \alpha_{xy}^{(k)} \end{Bmatrix} \right) dz dA \tag{1}$$

Notice in Eq. (1) the integral over the in-plane parent element domain A and the integral along the thickness of any given layer k in the interval $[z_k, z_{k+1}]$. The number of Gaussian integration points required to integrate over A is determined by the bending interpolation functions. In the case of the triangular BCIZ element, a complete polynomial of third degree with 10 coefficients is used, requiring the 13-point formula [5]. In the case of the quadrilateral element, a complete polynomial up to the terms of third degree and incomplete in the fourth degree ($\xi^3\eta$ and $\xi\eta^3$) is used, requiring 4-point formula along ξ and 4-point formula along η [6].

An alternative to the numerical integration along $[z_k, z_{k+1}]$ exits. Interpolation functions and their derivatives appear in matrices $\mathbf{B}^{(k)}$ of Eq. (1). Hence, it is possible to split these matrices into parts of increasing order. For instance, if a global cubic interpolation along z is adopted then $\mathbf{B}^{(k)} = \mathbf{B}_0{}^{(k)} + \zeta \mathbf{B}_1{}^{(k)} + \zeta^2 \mathbf{B}_2{}^{(k)} + \zeta^3 \mathbf{B}_3{}^{(k)}$. Observe that the $\mathbf{B}^{(k)}$ matrices also depend on the local interpolation functions. Assuming that the 2–3 superposition theory is used (elements types B, D or F), one would have $H_0 = {\zeta_k}^2$, $H_1 = {\zeta_k}^3$. Since the relationship $\zeta_k = (\zeta h - z_k - z_{k+1})/h_k$ holds, where h is the total laminate thickness and h_k is the thickness of layer k, the local functions H_0 and H_1 can also be split into constant, linear, quadratic and cubic terms in ζ. Substitution in Eq. (1) leads to the appearance of laminate matrices $\mathbf{A}_0$–$\mathbf{A}_6$ of the form

$$(\mathbf{A}_0, \mathbf{A}_1, \mathbf{A}_2, \mathbf{A}_3, \mathbf{A}_4, \mathbf{A}_5, \mathbf{A}_6) = \sum_{k=0}^{n-1} \int_{z_k}^{z_{k+1}} (1, \zeta, \zeta^2, \zeta^3, \zeta^4, \zeta^5, \zeta^6) \mathbf{C}^{(k)} dz \tag{2}$$

that can be analytically computed, eliminating the need for numerical integration along z.

Since the element implemented has 3D capabilities, the material properties that must be known are: moduli of elasticity in the principal directions ${E_1}^{(k)}$, ${E_2}^{(k)}$, ${E_3}^{(k)}$; shear moduli ${G_{23}}^{(k)}$, ${G_{13}}^{(k)}$, ${G_{12}}^{(k)}$; Poisson coefficients ${\nu_{23}}^{(k)}$, ${\nu_{32}}^{(k)}$, ${\nu_{13}}^{(k)}$, ${\nu_{31}}^{(k)}$, ${\nu_{12}}^{(k)}$, ${\nu_{21}}^{(k)}$; and coefficients of thermal expansion ${\alpha_1}^{(k)}$, ${\alpha_2}^{(k)}$, ${\alpha_3}^{(k)}$. The material stiffness matrix in the principal axes, $\mathbf{Q}^{(k)}$, for layer k is:

Table 1 Element types with global and local transverse interpolation functions

Element	${u_G}^{(k)}(z)$	${v_G}^{(k)}(z)$	${w_G}^{(k)}(z)$	${u_L}^{(k)}(\zeta_k)$	${v_L}^{(k)}(\zeta_k)$	${w_L}^{(k)}(\zeta_k)$
A	Linear	Linear	Linear	$\zeta_k, {\zeta_k}^2$	$\zeta_k, {\zeta_k}^2$	$\zeta_k, {\zeta_k}^2$
B	Linear	Linear	Linear	${\zeta_k}^2, {\zeta_k}^3$	${\zeta_k}^2, {\zeta_k}^3$	${\zeta_k}^2, {\zeta_k}^3$
C	Quadratic	Quadratic	Quadratic	$\zeta_k, {\zeta_k}^2$	$\zeta_k, {\zeta_k}^2$	$\zeta_k, {\zeta_k}^2$
D	Quadratic	Quadratic	Quadratic	${\zeta_k}^2, {\zeta_k}^3$	${\zeta_k}^2, {\zeta_k}^3$	${\zeta_k}^2, {\zeta_k}^3$
E	Cubic	Cubic	Cubic	$\zeta_k, {\zeta_k}^2$	$\zeta_k, {\zeta_k}^2$	$\zeta_k, {\zeta_k}^2$
F	Cubic	Cubic	Cubic	${\zeta_k}^2, {\zeta_k}^3$	${\zeta_k}^2, {\zeta_k}^3$	${\zeta_k}^2, {\zeta_k}^3$

$$\mathbf{Q}^{(k)} = \begin{bmatrix} Q_{11}^{(k)} & Q_{12}^{(k)} & Q_{13}^{(k)} & 0 & 0 & 0 \\ Q_{12}^{(k)} & Q_{22}^{(k)} & Q_{23}^{(k)} & 0 & 0 & 0 \\ Q_{13}^{(k)} & Q_{23}^{(k)} & Q_{33}^{(k)} & 0 & 0 & 0 \\ 0 & 0 & 0 & Q_{44}^{(k)} & 0 & 0 \\ 0 & 0 & 0 & 0 & Q_{55}^{(k)} & 0 \\ 0 & 0 & 0 & 0 & 0 & Q_{66}^{(k)} \end{bmatrix} \tag{3}$$

where $Q_{11}^{(k)} = (1 - \nu_{23}^{(k)}\nu_{32}^{(k)})/(E_2^{(k)}E_3^{(k)}\mu^{(k)})$, $Q_{22}^{(k)} = (1 - \nu_{13}^{(k)}\nu_{31}^{(k)})/(E_1^{(k)}E_3^{(k)}\mu^{(k)})$, $Q_{33}^{(k)} = (1 - \nu_{12}^{(k)}\nu_{21}^{(k)})/(E_1^{(k)}E_2^{(k)}\mu^{(k)})$, $Q_{12}^{(k)} = (\nu_{12}^{(k)} + \nu_{32}^{(k)}\nu_{13}^{(k)})/(E_1^{(k)}E_3^{(k)}\mu^{(k)})$, $Q_{13}^{(k)} = (\nu_{13}^{(k)} + \nu_{12}^{(k)}\nu_{23}^{(k)})/(E_1^{(k)}E_2^{(k)}\mu^{(k)})$, $Q_{23}^{(k)} = (\nu_{23}^{(k)} + \nu_{21}^{(k)}\nu_{13}^{(k)})/(E_2^{(k)}E_3^{(k)}\mu^{(k)})$, $Q_{44}^{(k)} = G_{23}^{(k)}$, $Q_{55}^{(k)} = G_{13}^{(k)}$, $Q_{66}^{(k)} = G_{12}^{(k)}$ and $\mu^{(k)} = (1 - \nu_{12}^{(k)}\nu_{21}^{(k)} - \nu_{13}^{(k)}\nu_{31}^{(k)} - \nu_{23}^{(k)}\nu_{32}^{(k)} - 2\nu_{21}^{(k)}\nu_{32}^{(k)}\nu_{13}^{(k)})/(E_1^{(k)}E_2^{(k)}E_3^{(k)})$.

The material stiffness matrix in the local element axes, $\mathbf{C}^{(k)}$, is

$$\mathbf{C}^{(k)} = \begin{bmatrix} C_{11}^{(k)} & C_{12}^{(k)} & C_{13}^{(k)} & 0 & 0 & C_{16}^{(k)} \\ C_{12}^{(k)} & C_{22}^{(k)} & C_{23}^{(k)} & 0 & 0 & C_{26}^{(k)} \\ C_{13}^{(k)} & C_{23}^{(k)} & C_{33}^{(k)} & 0 & 0 & C_{36}^{(k)} \\ 0 & 0 & 0 & C_{44}^{(k)} & C_{45}^{(k)} & 0 \\ 0 & 0 & 0 & C_{45}^{(k)} & C_{55}^{(k)} & 0 \\ C_{16}^{(k)} & C_{26}^{(k)} & C_{36}^{(k)} & 0 & 0 & C_{66}^{(k)} \end{bmatrix} \tag{4}$$

where the lamination angle of layer k is θ_k, $s = \sin\theta_k$, $c = \cos\theta k$, and

$$\begin{aligned}
C_{11}^{(k)} &= Q_{11}^{(k)}c^4 + Q_{22}^{(k)}s^4 + 2c^2s^2Q_{12}^{(k)} + 4c^2s^2Q_{66}^{(k)} \\
C_{12}^{(k)} &= (Q_{11}^{(k)} + Q_{22}^{(k)})c^2s^2 + Q_{12}^{(k)}(c^4 + s^4) - 4c^2s^2Q_{66}^{(k)} \\
C_{13}^{(k)} &= Q_{13}^{(k)}c^2 + Q_{23}^{(k)}s^2,\ C_{23}^{(k)} = Q_{13}^{(k)}s^2 + Q_{23}^{(k)}c^2 \\
C_{16}^{(k)} &= (Q_{11}^{(k)} - Q_{12}^{(k)})c^3s + (Q_{12}^{(k)} - Q_{22}^{(k)})cs^3 - 2cs(c^2 - s^2)Q_{66}^{(k)} \\
C_{22}^{(k)} &= Q_{11}^{(k)}s^4 + Q_{22}^{(k)}c^4 + 2c^2s^2Q_{12}^{(k)} + 4c^2s^2Q_{66}^{(k)} \\
C_{26}^{(k)} &= (Q_{11}^{(k)} - Q_{12}^{(k)})cs^3 + (Q_{12}^{(k)} - Q_{22}^{(k)})c^3s + 2cs(c^2 - s^2)Q_{66}^{(k)} \\
C_{33}^{(k)} &= Q_{33}^{(k)},\ C_{36}^{(k)} = (Q_{13}^{(k)} - Q_{23}^{(k)})cs \\
C_{44}^{(k)} &= Q_{44}^{(k)}c^2 + Q_{55}^{(k)}s^2,\ C_{45}^{(k)} = (Q_{55}^{(k)} - Q_{44}^{(k)})cs,\ C_{55}^{(k)} = Q_{44}^{(k)}s^2 + Q_{55}^{(k)}c^2 \\
C_{66}^{(k)} &= (Q_{11}^{(k)} + Q_{22}^{(k)} - 2Q_{12}^{(k)})c^2s^2 + Q_{66}^{(k)}(c^2 - s^2)^2
\end{aligned} \tag{5}$$

The lamination angle of layer k is θ_k measured with respect to side 1–2 of the element. Figure 4 in part I illustrates the local coordinate system xyz of both tria and quad elements. The x axis is aligned with side 1–2, but it does not have to be. In practical implementation the orientation of the element local coordinate system is determined though the procedure presented in the next section.

3 The plate bending elements

The purpose of this section is to clearly present the implementations of the elements with their in-plane, bending and drilling interpolation functions.

3.1 The triangular plate bending element

The three-node triangle plate bending element to be implemented is shown in Fig. 1 with the mapping from local ($\xi\eta$) to element coordinates (xy). The traditional area coordinates are ξ, η and $\varsigma = 1 - \xi - \eta$. The central node 0 can be subsequently eliminated.

Since plate bending behavior is to be modeled, nodes 1–3 possess each six degrees of freedom: u, v, w, $w_{,\xi}$, $w_{,\eta}$ and the drilling θ_z, whereas node 0 possesses only three degrees of freedom: u, v and w. Therefore, there is a total of 21 degrees of freedom. Notice that, in the element coordinate system, the rotational degrees of freedom $w_{,\xi}$ and $w_{,\eta}$ must be computed in terms of the local coordinates x and y, i.e., $w_{,x}$ and $w_{,y}$. This can be accomplished by the chain rule of differentiation:

$$\begin{Bmatrix} w_{,\xi} \\ w_{,\eta} \end{Bmatrix} = \begin{bmatrix} x_{,\xi} & y_{,\xi} \\ x_{,\eta} & y_{,\eta} \end{bmatrix} \begin{Bmatrix} w_{,x} \\ w_{,y} \end{Bmatrix} \tag{6}$$

and the derivatives of x and y with respect to ξ and η can be obtained using the nodal coordinates (x_i, y_i) and the area coordinates:

$$x = \xi x_1 + \eta x_2 + \varsigma x_3, \quad y = \xi y_1 + \eta y_2 + \varsigma y_3 \tag{7}$$

The interpolation scheme proposed for u and v is quadratic and given by

$$u = \sum_{i=0}^{3} \varphi_i u_i + \sum_{i=1}^{3} P_{ui}\theta_{zi}, \quad v = \sum_{i=0}^{3} \varphi_i v_i + \sum_{i=1}^{3} P_{vi}\theta_{zi} \tag{8}$$

where

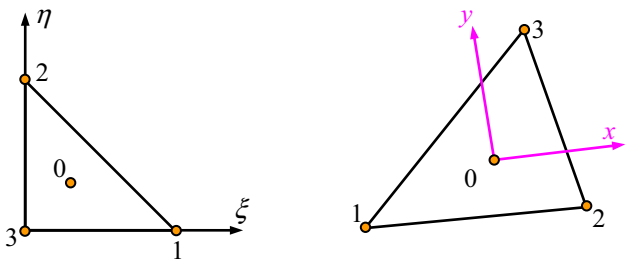

Fig. 1 Three-node element topology and mapping

$$\varphi_1 = \xi - \xi\eta - \xi\varsigma - \eta\varsigma,\ \varphi_2 = \eta - \xi\eta - \xi\varsigma - \eta\varsigma,$$
$$\varphi_3 = \zeta - \xi\eta - \xi\varsigma - \eta\varsigma,\ \varphi_0 = 3(\xi\eta + \xi\varsigma + \eta\varsigma) \tag{9}$$

and the drilling interpolation functions are those presented in Eq. (36) of part I [7]. The interpolation scheme proposed for w consists in a complete polynomial of third degree with 10 coefficients:

$$w(\xi,\eta) = a_0 + a_1\xi + a_2\eta + a_3\xi^2 + a_4\xi\eta + a_5\eta^2 + a_6\xi^3 + a_7\xi^2\eta + a_8\xi\eta^2 + a_9\eta^3 \tag{10}$$

The 10 coefficients in Eq. (10) can be determined by imposition of the conditions given in Table 2, leading to the interpolation for w in terms of shape functions N_1-N10 and the nodal degrees of freedom w_1, $w_{1,\xi}$, $w_{1,\eta}$, w_2, $w_{2,\xi}$, $w_{2,\eta}$, w_3, $w_{3,\xi}$, $w_{3,\eta}$, w_0:

$$w = N_1 w_1 + N_2^{**} w_{1,\xi} + N_3^{**} w_{1,\eta} + N_4 w_2 + N_5^{**} w_{2,\xi} + N_6^{**} w_{2,\eta} + N_7 w_3 + N_8^{**} w_{3,\xi} + N_9^{**} w_{3,\eta} + N_{10} w_0 \tag{11}$$

where

$$N_1 = 3\xi^2 - 2\xi^3 - 7\xi\eta\varsigma,\ N_2^{**} = -\xi^2 + \xi^3 + 2\xi\eta\varsigma,\ N_3^{**} = \xi^2\eta - \xi\eta\varsigma \tag{12}$$

$$N_4 = 3\eta^2 - 2\eta^3 - 7\xi\eta\varsigma,\ N_5^{**} = \xi\eta^2 - 2\xi\eta\varsigma,\ N_6^{**} = -\eta^2 + \eta^3 + 2\xi\eta\varsigma \tag{13}$$

$$N_7 = 3\varsigma^2 - 2\varsigma^3 - 7\xi\eta\varsigma,\ N_8^{**} = \xi\varsigma^2 - \xi\eta\varsigma,\ N_9^{**} = \eta\varsigma^2 - \xi\eta\varsigma \tag{14}$$

$$N_{10} = 27\xi\eta\varsigma \tag{15}$$

According to Eq. (6), the second and third terms in Eq. (11) are written as

$$\begin{aligned} N_2^{**} w_{1,\xi} + N_3^{**} w_{1,\eta} &= N_2^{**}(x_{1,\xi} w_{1,x} + y_{1,\xi} w_{1,y}) + N_3^{**}(x_{1,\eta} w_{1,x} + y_{1,\eta} w_{1,y}) \\ &= (N_2^{**} x_{1,\xi} + N_3^{**} x_{1,\eta}) w_{1,x} + (N_2^{**} y_{1,\xi} + N_3^{**} y_{1,\eta}) w_{1,y} \\ &= N_2^{*} w_{1,x} + N_3^{*} w_{1,y} \end{aligned} \tag{16}$$

where $x_{1,\xi}$, $y_{1,\xi}$, $x_{1,\eta}$ and $y_{1,\eta}$ are the terms of the Jacobian matrix. Since the mapping is linear, the Jacobian matrix is constant and $x_{,\xi} = x_{13}$, $y_{,\xi} = y_{13}$, $x_{,\eta} = x_{23}$ and $y_{,\eta} = y_{23}$, where $x_{ij} = x_i - x_j$ and $y_{ij} = y_i - y_j$. Hence, $N_2^{*} = N_2^{**} x_{13} + N_3^{**} x_{23}$ and $N_3^{*} = N_2^{**} y_{13} + N_3^{**} y_{23}$. Moreover, rotational degrees of freedom are usually defined as $\theta_x = w_{,y}$ and $\theta_y = -w_{,x}$, such that $N_2 = N_3^{*}$ and $N_3 = -N_2^{*}$. The new interpolation function for w in terms of θ_x and θ_y is

$$w = N_1 w_1 + N_2\theta_{x1} + N_3\theta_{y1} + N_4 w_2 + N_5\theta_{x2} + N_6\theta_{y2} + N_7 w_3 + N_8\theta_{x3} + N_9\theta_{y3} + N_{10} w_0 \tag{17}$$

Second derivatives of w are required in the computation of strains. These can be evaluated through double application of the chain rule yielding

$$\begin{Bmatrix} w_{,\xi\xi} \\ w_{,\xi\eta} \\ w_{,\eta\eta} \end{Bmatrix} = \begin{bmatrix} x_{,\xi}^2 & 2x_{,\xi}y_{,\xi} & y_{,\xi}^2 \\ x_{,\xi}x_{,\eta} & x_{,\xi}y_{,\eta} + x_{,\eta}y_{,\xi} & y_{,\xi}y_{,\eta} \\ x_{,\eta}^2 & 2x_{,\eta}y_{,\eta} & y_{,\eta}^2 \end{bmatrix} \begin{Bmatrix} w_{,xx} \\ w_{,xy} \\ w_{,yy} \end{Bmatrix} + \begin{bmatrix} x_{,\xi\xi} & y_{,\xi\xi} \\ x_{,\xi\eta} & y_{,\xi\eta} \\ x_{,\eta\eta} & y_{,\eta\eta} \end{bmatrix} \begin{Bmatrix} w_{,x} \\ w_{,y} \end{Bmatrix} \tag{18}$$

and, since the Jacobian matrix is constant, $x_{,\xi\xi} = y_{,\xi\xi} = x_{,\xi\eta} = y_{,\xi\eta} = x_{,\eta\eta} = y_{,\eta\eta} = 0$, leading to

$$\begin{aligned} \begin{Bmatrix} w_{,xx} \\ w_{,xy} \\ w_{,yy} \end{Bmatrix} &= \begin{bmatrix} x_{,\xi}^2 & 2x_{,\xi}y_{,\xi} & y_{,\xi}^2 \\ x_{,\xi}x_{,\eta} & x_{,\xi}y_{,\eta} + x_{,\eta}y_{,\xi} & y_{,\xi}y_{,\eta} \\ x_{,\eta}^2 & 2x_{,\eta}y_{,\eta} & y_{,\eta}^2 \end{bmatrix}^{-1} \begin{Bmatrix} w_{,\xi\xi} \\ w_{,\xi\eta} \\ w_{,\eta\eta} \end{Bmatrix} \\ &= \begin{bmatrix} x_{13}^2 & 2x_{13}y_{13} & y_{13}^2 \\ x_{13}x_{23} & x_{13}y_{23} + x_{23}y_{13} & y_{13}y_{23} \\ x_{23}^2 & 2x_{23}y_{23} & y_{23}^2 \end{bmatrix}^{-1} \begin{Bmatrix} w_{,\xi\xi} \\ w_{,\xi\eta} \\ w_{,\eta\eta} \end{Bmatrix} \end{aligned} \tag{19}$$

However, when the degree of freedom w_0 is condensed out, the resulting element becomes too stiff under bending since the curvature completeness is lost. In order to overcome this problem, the BCIZ element was implemented. Its idea is to still condense out w_0 but maintaining curvature completeness. Consider the six node quadratic element shown in Fig. 2 whose interpolation functions are

$$\psi_1 = \xi(2\xi - 1),\ \psi_2 = \eta(2\eta - 1),\ \psi_3 = \zeta(2\varsigma - 1),$$
$$\psi_4 = 4\xi\eta,\ \psi_5 = 4\eta\varsigma,\ \psi_6 = 4\xi\varsigma \tag{20}$$

One can express w_0 (the transverse displacement in the center of the element) in terms of the nodal transverse

Table 2 Conditions to be imposed in the determination of the interpolation for w in the triangular element

Node	ξ	η	ς	w	$w_{,\xi}$	$w_{,\eta}$
1	1	0	0	w_1	$w_{1,\xi}$	$w_{1,\eta}$
2	0	1	0	w_2	$w_{2,\xi}$	$w_{2,\eta}$
3	0	0	1	w_3	$w_{3,\xi}$	$w_{3,\eta}$
0	1/3	1/3	1/3	w_0	–	–

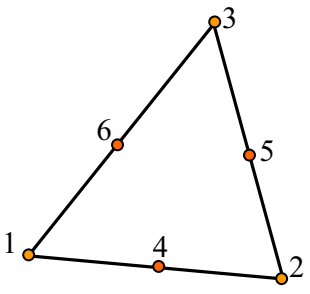

Fig. 2 Quadratic interpolation for w

displacements w_1-w_6 through the use of the interpolations functions defined in Eq. (20) evaluated at $\xi=\eta=\varsigma=1/3$:

$$w_0 = \frac{4}{9}(w_4 + w_5 + w_6) - \frac{1}{9}(w_1 + w_2 + w_3) \tag{21}$$

Next, the interpolation functions defined in Eq. (17) can be used to compute w_4, w_5 and w_6 in terms of the degrees of freedom w_1, θ_{x1}, θ_{y1}, w_2, θ_{x2}, θ_{y2}, w_3, θ_{x3}, θ_{y3}. w_4 is computed making $\xi=\eta=1/2$ and $\varsigma=0$. w_5 is computed making $\eta=\varsigma=1/2$ and $\xi=0$. w_6 is computed making $\xi=\varsigma=1/2$ and $\eta=0$. Hence,

$$\begin{aligned}
w_4 &= \frac{w_1}{2} + \frac{y_{21}}{8}\theta_{x1} - \frac{x_{21}}{8}\theta_{y1} + \frac{w_2}{2} - \frac{y_{21}}{8}\theta_{x2} + \frac{x_{21}}{8}\theta_{y2} \\
w_5 &= \frac{w_2}{2} + \frac{y_{32}}{8}\theta_{x2} - \frac{x_{32}}{8}\theta_{y2} + \frac{w_3}{2} - \frac{y_{32}}{8}\theta_{x3} + \frac{x_{32}}{8}\theta_{y3} \\
w_6 &= \frac{w_1}{2} - \frac{y_{13}}{8}\theta_{x1} + \frac{x_{13}}{8}\theta_{y1} + \frac{w_3}{2} + \frac{y_{13}}{8}\theta_{x3} - \frac{x_{13}}{8}\theta_{y3}
\end{aligned} \tag{22}$$

Substitution of Eq. (22) into (21) gives

$$\begin{aligned}
w_0 = {} & \frac{1}{3}(w_1 + w_2 + w_3) + \frac{y_{21} - y_{13}}{18}\theta_{x1} + \frac{x_{13} - x_{21}}{18}\theta_{y1} \\
& + \frac{y_{32} - y_{21}}{18}\theta_{x2} + \frac{x_{21} - x_{32}}{18}\theta_{y2} + \frac{y_{13} - y_{32}}{18}\theta_{x3} + \frac{x_{32} - x_{13}}{18}\theta_{y3}
\end{aligned} \tag{23}$$

Equation (23) can now be substituted into Eq. (17) to eliminate w_0 yielding

$$\begin{aligned}
w = {} & (N_1 + a_{w1}N_{10})w_1 + (N_2 + a_{\theta x1}N_{10})\theta_{x1} + (N_3 + a_{\theta y1}N_{10})\theta_{y1} \\
& + (N_4 + a_{w2}N_{10})w_2 + (N_5 + a_{\theta x2}N_{10})\theta_{x2} + (N_6 + a_{\theta y2}N_{10})\theta_{y2} \\
& + (N_7 + a_{w3}N_{10})w_3 + (N_8 + a_{\theta x3}N_{10})\theta_{x3} + (N_9 + a_{\theta y3}N_{10})\theta_{y3}
\end{aligned} \tag{24}$$

where $a_{w1} = a_{w2} = a_{w3} = 1/3$, $a_{\theta x1} = (y_{21} - y_{13})/18$, $a_{\theta y1} = (x_{13} - x_{21})/18$, $a_{\theta x2} = (y_{32} - y_{21})/18$, $a_{\theta y2} = (x_{21} - x_{32})/18$, $a_{\theta x3} = (y_{13} - y_{32})/18$, $a_{\theta y3} = (x_{32} - x_{13})/18$. The implementation of the element proceeds normally using the interpolation functions for w defined in Eq. (24).

3.2 The quadrilateral plate bending element

The four-node plate bending element to be implemented is shown in Fig. 3 with the mapping from local ($\xi\eta$) to element coordinates (xy).

Since plate bending behavior is to be modeled, nodes 1–4 possess each six degrees of freedom: u, v, w, $w_{,\xi}$, $w_{,\eta}$ and the drilling θ_z. Therefore, there is a total of 24 degrees of freedom. Notice that, in the element coordinate system, the rotational degrees of freedom $w_{,\xi}$ and $w_{,\eta}$ must be computed in terms of the coordinates x and y, i.e., $w_{,x}$ and $w_{,y}$. This can be accomplished by the chain rule of differentiation as in Eq. (6). The derivatives of x and y with respect to ξ and η

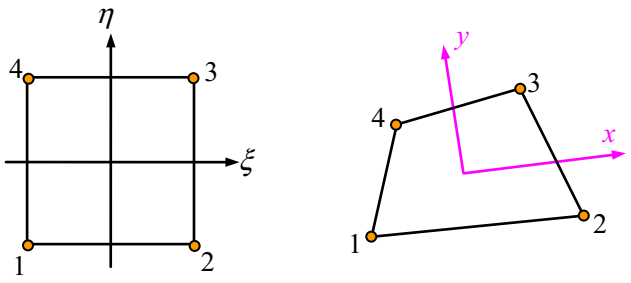

Fig. 3 Four-node element topology and mapping

can be obtained using the nodal coordinates (x_i, y_i) and the bilinear Lagrange interpolation functions:

$$x = \sum_{i=1}^{4} \varphi_i x_i, \; y = \sum_{i=1}^{4} \varphi_i y_i \tag{25}$$

The interpolation scheme proposed for u and v is given by

$$u = \sum_{i=1}^{4} (\varphi_i u_i + P_{ui}\theta_{zi}), \; v = \sum_{i=1}^{4} (\varphi_i v_i + P_{vi}\theta_{zi}) \tag{26}$$

where

$$\begin{aligned}
\varphi_1 &= \frac{1}{4}(1-\xi)(1-\eta), \; \varphi_2 = \frac{1}{4}(1+\xi)(1-\eta), \\
\varphi_3 &= \frac{1}{4}(1+\xi)(1+\eta), \; \varphi_4 = \frac{1}{4}(1-\xi)(1+\eta)
\end{aligned} \tag{27}$$

and the drilling interpolation functions are [8]

$$\begin{aligned}
P_{u1} &= \frac{1}{16}[l_{41}(1-\xi)(1-\eta^2)\sin\beta_{41} - l_{12}(1-\xi^2)(1-\eta)\sin\beta_{12}] \\
P_{v1} &= \frac{1}{16}[l_{12}(1-\xi^2)(1-\eta)\cos\beta_{12} - l_{41}(1-\xi)(1-\eta^2)\cos\beta_{41}] \\
P_{u2} &= \frac{1}{16}[l_{12}(1-\xi^2)(1-\eta)\sin\beta_{12} - l_{23}(1+\xi)(1-\eta^2)\sin\beta_{23}] \\
P_{v2} &= \frac{1}{16}[l_{23}(1+\xi)(1-\eta^2)\cos\beta_{23} - l_{12}(1-\xi^2)(1-\eta)\cos\beta_{12}] \\
P_{u3} &= \frac{1}{16}[l_{23}(1+\xi)(1-\eta^2)\sin\beta_{23} - l_{34}(1-\xi^2)(1+\eta)\sin\beta_{34}] \\
P_{v3} &= \frac{1}{16}[l_{34}(1-\xi^2)(1+\eta)\cos\beta_{34} - l_{23}(1+\xi)(1-\eta^2)\cos\beta_{23}] \\
P_{u4} &= \frac{1}{16}[l_{34}(1-\xi^2)(1+\eta)\sin\beta_{34} - l_{41}(1-\xi)(1-\eta^2)\sin\beta_{41}] \\
P_{v4} &= \frac{1}{16}[l_{41}(1-\xi)(1-\eta^2)\cos\beta_{41} - l_{34}(1-\xi^2)(1+\eta)\cos\beta_{34}]
\end{aligned} \tag{28}$$

The interpolation scheme proposed for w consists in a polynomial of fourth degree with 12 coefficients. The polynomial is complete up to term of third degree and incomplete in the fourth degree:

Table 3 Conditions to be imposed in the determination of the interpolation for w in the quadrilateral element

Node	ξ	η	w	$w_{,\xi}$	$w_{,\eta}$
1	−1	−1	w_1	$w_{1,\xi}$	$w_{1,\eta}$
2	1	−1	w_2	$w_{2,\xi}$	$w_{2,\eta}$
3	1	1	w_3	$w_{3,\xi}$	$w_{3,\eta}$
4	−1	1	w_4	$w_{4,\xi}$	$w_{4,\eta}$

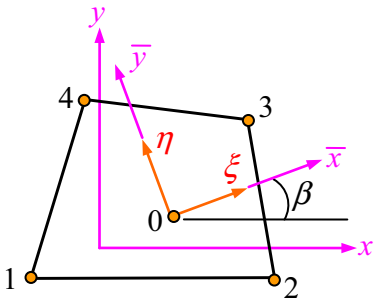

Fig. 4 Four-node element topology and mapping

$$w(\xi,\eta) = a_0 + a_1\xi + a_2\eta + a_3\xi^2 + a_4\xi\eta + a_5\eta^2 + a_6\xi^3 + a_7\xi^2\eta + a_8\xi\eta^2 + a_9\eta^3 + a_{10}\xi^3\eta + a_{11}\xi\eta^3 \quad (29)$$

The 12 coefficients in Eq. (29) can be determined by imposition of the conditions given in Table 3, leading to the interpolation for w in terms of shape functions N_1-N_{12} and the nodal degrees of freedom w_1, $w_{1,\xi}$, $w_{1,\eta}$, …, w_4, $w_{4,\xi}$, $w_{4,\eta}$:

$$w = N_1 w_1 + N_2^{**} w_{1,\xi} + N_3^{**} w_{1,\eta} + \cdots + N_{10} w_4 + N_{11}^{**} w_{4,\xi} + N_{12}^{**} w_{4,\eta} \quad (30)$$

where

$$N_1 = \frac{1}{8}(2 - 3\xi - 3\eta + 4\xi\eta + \xi^3 + \eta^3 - \xi^3\eta - \xi\eta^3)$$
$$N_2^{**} = \frac{1}{8}(1 - \xi - \eta - \xi^2 + \xi\eta + \xi^3 + \xi^2\eta - \xi^3\eta) \quad (31)$$
$$N_3^{**} = \frac{1}{8}(1 - \xi - \eta + \xi\eta - \eta^2 + \xi\eta^2 + \eta^3 - \xi\eta^3)$$

$$N_4 = \frac{1}{8}(2 + 3\xi - 3\eta - 4\xi\eta - \xi^3 + \eta^3 + \xi^3\eta + \xi\eta^3)$$
$$N_5^{**} = \frac{1}{8}(-1 - \xi + \eta + \xi^2 + \xi\eta + \xi^3 - \xi^2\eta - \xi^3\eta) \quad (32)$$
$$N_6^{**} = \frac{1}{8}(1 + \xi - \eta - \xi\eta - \eta^2 - \xi\eta^2 + \eta^3 + \xi\eta^3)$$

$$N_7 = \frac{1}{8}(2 + 3\xi + 3\eta + 4\xi\eta - \xi^3 - \eta^3 - \xi^3\eta - \xi\eta^3)$$
$$N_8^{**} = \frac{1}{8}(-1 - \xi - \eta + \xi^2 - \xi\eta + \xi^3 + \xi^2\eta + \xi^3\eta) \quad (33)$$
$$N_9^{**} = \frac{1}{8}(-1 - \xi - \eta - \xi\eta + \eta^2 + \xi\eta^2 + \eta^3 + \xi\eta^3)$$

$$N_{10} = \frac{1}{8}(2 - 3\xi + 3\eta - 4\xi\eta + \xi^3 - \eta^3 + \xi^3\eta + \xi\eta^3)$$
$$N_{11}^{**} = \frac{1}{8}(1 - \xi + \eta - \xi^2 - \xi\eta + \xi^3 - \xi^2\eta + \xi^3\eta) \quad (34)$$
$$N_{12}^{**} = \frac{1}{8}(-1 + \xi - \eta + \xi\eta + \eta^2 - \xi\eta^2 + \eta^3 - \xi\eta^3)$$

According to Eq. (6), the second and third terms in Eq. (30) are written as

$$N_2^{**} w_{1,\xi} + N_3^{**} w_{1,\eta} = N_2^{**}(x_{1,\xi} w_{1,x} + y_{1,\xi} w_{1,y}) + N_3^{**}(x_{1,\eta} w_{1,x} + y_{1,\eta} w_{1,y}) = (N_2^{**} x_{1,\xi} + N_3^{**} x_{1,\eta}) w_{1,x} + (N_2^{**} y_{1,\xi} + N_3^{**} y_{1,\eta}) w_{1,y} = N_2^{*} w_{1,x} + N_3^{*} w_{1,y} \quad (35)$$

where $x_{1,\xi}$, $y_{1,\xi}$, $x_{1,\eta}$ and $y_{1,\eta}$ are the terms of the Jacobian matrix evaluated at node 1. For the nodes 2–4, it is also possible to write expressions similar to Eq. (35) leading to the modified interpolation function for w in terms of $w_{,x}$ and $w_{,y}$. Moreover, rotational degrees of freedom are usually defined as $\theta_x = w_{,y}$ and $\theta_y = -w_{,x}$, such that $N_2 = N_3^{*}$ and $N_3 = -N_2^{*}$. The new interpolation function for w in terms of θ_x and θ_y is

$$w = N_1 w_1 + N_2 \theta_{x1} + N_3 \theta_{y1} + \cdots + N_{10} w_4 + N_{11} \theta_{x4} + N_{12} \theta_{y4} \quad (36)$$

Second-order derivatives of w are required in the computation of strains. These can be evaluated through double application of the chain rule yielding Eq. (18). Similarly, third-order derivatives $w_{,xxx}$, $w_{,xxy}$, $w_{,xyy}$ and $w_{,yyy}$ can be evaluated as

$$\begin{Bmatrix} w_{,\xi\xi\xi} \\ w_{,\xi\xi\eta} \\ w_{,\xi\eta\eta} \\ w_{,\eta\eta\eta} \end{Bmatrix} = \begin{bmatrix} x_{,\xi}^3 & 3x_{,\xi}^2 y_{,\xi} & 3x_{,\xi} y_{,\xi}^2 & y_{,\xi}^3 \\ x_{,\xi}^2 x_{,\eta} & x_{,\xi}^2 y_{,\eta} + 2x_{,\xi} x_{,\eta} y_{,\xi} & 2x_{,\xi} y_{,\xi} y_{,\eta} + x_{,\eta} y_{,\xi}^2 & y_{,\xi}^2 y_{,\eta} \\ x_{,\xi} x_{,\eta}^2 & x_{,\eta}^2 y_{,\xi} + 2x_{,\xi} x_{,\eta} y_{,\eta} & x_{,\xi} y_{,\eta}^2 + 2x_{,\eta} y_{,\xi} y_{,\eta} & y_{,\xi} y_{,\eta}^2 \\ x_{,\eta}^3 & 3x_{,\eta}^2 y_{,\eta} & 3x_{,\eta} y_{,\eta}^2 & y_{,\eta}^3 \end{bmatrix} \begin{Bmatrix} w_{,xxx} \\ w_{,xxy} \\ w_{,xyy} \\ w_{,yyy} \end{Bmatrix} + \begin{bmatrix} 3x_{,\xi} x_{,\xi\xi} & 3(x_{,\xi\xi} y_{,\xi} + x_{,\xi} y_{,\xi\xi}) & 3y_{,\xi} y_{,\xi\xi} \\ 2x_{,\xi} x_{,\xi\eta} + x_{,\xi\xi} x_{,\eta} & 2(x_{,\xi\eta} y_{,\xi} + x_{,\xi} y_{,\xi\eta}) + x_{,\xi\xi} y_{,\eta} + x_{,\eta} y_{,\xi\xi} & 2y_{,\xi} y_{,\xi\eta} + y_{,\xi\xi} y_{,\eta} \\ 2x_{,\eta} x_{,\xi\eta} + x_{,\xi} x_{,\eta\eta} & 2(x_{,\xi\eta} y_{,\eta} + x_{,\eta} y_{,\xi\eta}) + x_{,\eta\eta} y_{,\xi} + x_{,\xi} y_{,\eta\eta} & 2y_{,\eta} y_{,\xi\eta} + y_{,\xi} y_{,\eta\eta} \\ 3x_{,\eta} x_{,\eta\eta} & 3(x_{,\eta} y_{,\eta\eta} + x_{,\eta\eta} y_{,\eta}) & 3y_{,\eta} y_{,\eta\eta} \end{bmatrix} \begin{Bmatrix} w_{,xx} \\ w_{,xy} \\ w_{,yy} \end{Bmatrix} + \begin{bmatrix} x_{,\xi\xi\xi} & y_{,\xi\xi\xi} \\ x_{,\xi\xi\eta} & y_{,\xi\xi\eta} \\ x_{,\xi\eta\eta} & y_{,\xi\eta\eta} \\ x_{,\eta\eta\eta} & y_{,\eta\eta\eta} \end{bmatrix} \begin{Bmatrix} w_{,x} \\ w_{,y} \end{Bmatrix} \quad (37)$$

4 A technique to minimize Jacobian variation in quadrilateral elements

Evaluation of the Jacobian of a mapping transformation is necessary in the most common finite element numerical procedures. If the Jacobian of the transformation is constant, then it is expected that the numerical integration, usually carried out using the Gaussian integration rule, will be more accurate because fractions of polynomials are avoided in the computation of strains. This document describes a procedure to make the Jacobian of a four-node quadrilateral element as constant as possible simply by selecting an appropriate local reference system. Since transformation of local to global reference systems is almost always inevitable, the procedure presented does not add significant burden to the numerical processing cost.

The topology of the four-node quadrilateral element is shown in Fig. 4. Originally, the local coordinate system assigned to this element is xy and the nodal coordinates in this original system are given by x_i, y_i, for $i=1, 2, 3, 4$. A new rotated local coordinate system can be defined as $\overline{xy}$ in which the nodal coordinates are $\bar{x}_i$, $\bar{y}_i$, for $i=1, 2, 3, 4$. The relationship between the two local reference systems is

$$\bar{x} = (x - x_0)\cos\beta + (y - y_0)\sin\beta,\ \bar{y} = (y - y_0)\cos\beta - (x - x_0)\sin\beta \tag{38}$$

where x_0, y_0 and β are parameters to be determined.

In the computation of strains, it is necessary to evaluate derivatives of displacements with respect to x and y, what can be accomplished by the chain rule of differentiation:

$$\begin{Bmatrix} \bar{u}_{,\xi} \\ \bar{u}_{,\eta} \end{Bmatrix} = \begin{bmatrix} \bar{x}_{,\xi} & \bar{y}_{,\xi} \\ \bar{x}_{,\eta} & \bar{y}_{,\eta} \end{bmatrix} \begin{Bmatrix} \bar{u}_{,x} \\ \bar{u}_{,y} \end{Bmatrix} \tag{39}$$

where $\bar{u}$ is the displacement along $\bar{x}$. In order to compute the elements of the 2×2 Jacobian matrix in Eq. (39), the required interpolation functions and their derivatives are

$$\begin{aligned} \varphi_1 &= \frac{1}{4}(1-\xi)(1-\eta),\ \varphi_2 = \frac{1}{4}(1+\xi)(1-\eta),\ \varphi_3 \\ &= \frac{1}{4}(1+\xi)(1+\eta),\ \varphi_4 = \frac{1}{4}(1-\xi)(1+\eta) \end{aligned} \tag{40}$$

$$\begin{aligned} \varphi_{1,\xi} &= \frac{1}{4}(\eta-1),\ \varphi_{2,\xi} = \frac{1}{4}(1-\eta), \\ \varphi_{3,\xi} &= \frac{1}{4}(1+\eta),\ \varphi_{4,\xi} = \frac{-1}{4}(1+\eta) \end{aligned} \tag{41}$$

$$\begin{aligned} \varphi_{1,\eta} &= \frac{1}{4}(\xi-1),\ \varphi_{2,\eta} = \frac{-1}{4}(1+\xi), \\ \varphi_{3,\eta} &= \frac{1}{4}(1+\xi),\ \varphi_{4,\eta} = \frac{1}{4}(1-\xi) \end{aligned} \tag{42}$$

The elements of the 2×2 Jacobian matrix are

$$\begin{aligned} \bar{x}_{,\xi} &= \frac{1}{4}[(\eta-1)\bar{x}_1 + (1-\eta)\bar{x}_2 + (1+\eta)\bar{x}_3 - (1+\eta)\bar{x}_4] \\ &= \frac{1}{4}[(-\bar{x}_1 + \bar{x}_2 + \bar{x}_3 - \bar{x}_4) + \eta(\bar{x}_1 - \bar{x}_2 + \bar{x}_3 - \bar{x}_4)] \end{aligned} \tag{43}$$

$$\begin{aligned} \bar{x}_{,\eta} &= \frac{1}{4}[(\xi-1)\bar{x}_1 - (1+\xi)\bar{x}_2 + (1+\xi)\bar{x}_3 + (1-\xi)\bar{x}_4] \\ &= \frac{1}{4}[(-\bar{x}_1 - \bar{x}_2 + \bar{x}_3 + \bar{x}_4) + \xi(\bar{x}_1 - \bar{x}_2 + \bar{x}_3 - \bar{x}_4)] \end{aligned} \tag{44}$$

$$\begin{aligned} \bar{y}_{,\xi} &= \frac{1}{4}[(\eta-1)\bar{y}_1 + (1-\eta)\bar{y}_2 + (1+\eta)\bar{y}_3 - (1+\eta)\bar{y}_4] \\ &= \frac{1}{4}[(-\bar{y}_1 + \bar{y}_2 + \bar{y}_3 - \bar{y}_4) + \eta(\bar{y}_1 - \bar{y}_2 + \bar{y}_3 - \bar{y}_4)] \end{aligned} \tag{45}$$

$$\begin{aligned} \bar{y}_{,\eta} &= \frac{1}{4}[(\xi-1)\bar{y}_1 - (1+\xi)\bar{y}_2 + (1+\xi)\bar{y}_3 + (1-\xi)\bar{y}_4] \\ &= \frac{1}{4}[(-\bar{y}_1 - \bar{y}_2 + \bar{y}_3 + \bar{y}_4) + \xi(\bar{y}_1 - \bar{y}_2 + \bar{y}_3 - \bar{y}_4)] \end{aligned} \tag{46}$$

Examination of Eqs. (43–46) permits to conclude that, in order for the Jacobian to be constant, the terms multiplied by both ξ and η must be zero, i.e., $\bar{x}_1 - \bar{x}_2 + \bar{x}_3 - \bar{x}_4 = 0$ and $\bar{y}_1 - \bar{y}_2 + \bar{y}_3 - \bar{y}_4 = 0$. However, both conditions cannot be rigorously met simultaneously. If one intuitively defines the quadratic error f as

$$f = (\bar{x}_1 - \bar{x}_2 + \bar{x}_3 - \bar{x}_4)^2 + (\bar{y}_1 - \bar{y}_2 + \bar{y}_3 - \bar{y}_4)^2 \tag{47}$$

and substitutes Eq. (38) into Eq. (47), the result is

$$f = (x_1 - x_2 + x_3 - x_4)^2 + (y_1 - y_2 + y_3 - y_4)^2 \tag{48}$$

or, the classical quadratic error is independent of x_0, y_0 and ϕ. Clearly, this is not a viable path. Another possibility is to recognize that a perfectly rectangular element, whose sides are parallel to the $\bar{x}$ and $\bar{y}$ axes, satisfies the four relations $\bar{x}_1 = \bar{x}_4$, $\bar{x}_2 = \bar{x}_3$, $\bar{y}_1 = \bar{y}_2$ and $\bar{y}_3 = \bar{y}_4$, leading to a constant Jacobian matrix. Thus, a new quadratic error g is now defined as

$$g = (\bar{x}_1 - \bar{x}_4)^2 + (\bar{x}_2 - \bar{x}_3)^2 + (\bar{y}_1 - \bar{y}_2)^2 + (\bar{y}_3 - \bar{y}_4)^2 \tag{49}$$

Substitution of Eq. (38) into Eq. (49) yields

$$\begin{aligned} g = {} & (x_{14}^2 + x_{23}^2 + y_{12}^2 + y_{34}^2)\frac{1+\cos 2\beta}{2} \\ & + (x_{21}^2 + x_{43}^2 + y_{14}^2 + y_{23}^2)\frac{1-\cos 2\beta}{2} \\ & + 2(x_{14}y_{14} + x_{23}y_{23} + x_{21}y_{12} + x_{43}y_{34})\frac{\sin 2\beta}{2} \end{aligned} \tag{50}$$

where $x_{ij}=x_i-x_j$ and $y_{ij}=y_i-y_j$. Notice that Eq. (50) is independent of x_0 and y_0. Enforcing $\partial g/\partial\beta=0$ leads to

$$\tan 2\beta = \frac{x_{13}y_{24} + x_{24}y_{13}}{x_{13}x_{24} - y_{13}y_{24}} \tag{51}$$

A good property of Eq. (51) is that the denominator $x_{13}x_{24} - y_{13}y_{24}$ is never zero, provided the quadrilateral element is not degenerated. Numerically, this is an advantage since the function at an can be used without further complications. As far as the parameters x_0 and y_0 are concerned, they can be arbitrarily selected as the centroid of the element, i.e., $x_0 = (x_1 + x_2 + x_3 + x_4)/4$ and $y_0 = (y_1 + y_2 + y_3 + y_4)/4$.

A geometrical interpretation for Eq. (51) can be given recognizing that the angle β_{13}, formed between diagonal 13 and the x axis, satisfies $\tan\beta_{13} = y_{13}/x_{13}$, and that the angle β_{24}, formed between diagonal 24 and the x axis, satisfies $\tan\beta_{24} = y_{24}/x_{24}$. Hence, Eq. (51) can be rewritten in the form

$$\tan 2\beta = \frac{\frac{y_{13}}{x_{13}} + \frac{y_{24}}{x_{24}}}{1 - \frac{y_{13}}{x_{13}}\frac{y_{24}}{x_{24}}} = \frac{\tan\beta_{13} + \tan\beta_{24}}{1 - \tan\beta_{13}\tan\beta_{24}} = \tan(\beta_{13} + \beta_{24}) \tag{52}$$

leading to the conclusion that $\beta = (\beta_{13} + \beta_{24})/2$, or that angle β is the angle formed between the bisector of the angle formed by the diagonals 13 and 24 and the x axis. This is precisely the orientation of the element coordinate system implemented in the Nastran CQUAD4 element.

As an example, the element with nodal coordinates $x_1 = 0$, $y_1 = 0$, $x_2 = 1$, $y_2 = 0$, $x_3 = 1$, $y_3 = 3$, $x_4 = -1$, $y_4 = 1$ is investigated. Straight use of Eq. (51) or (52) reveals that $\beta = 22.5°$. The quadratic error function g in Eq. (50) is computed for different values of β and plotted in Fig. 5, where a substantial variation of the error can be observed.

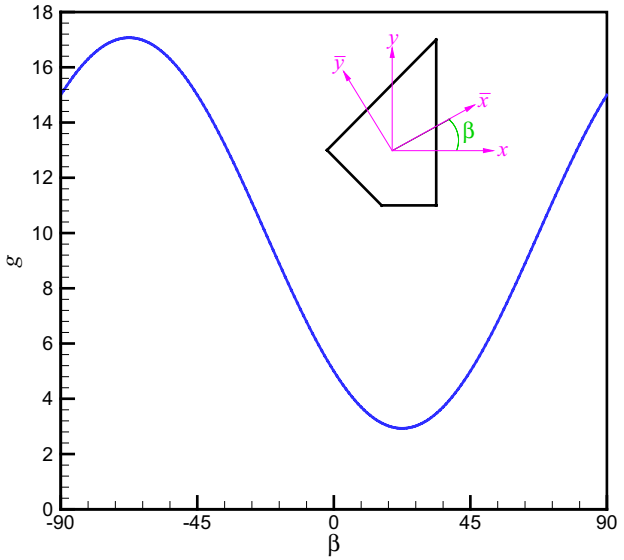

Fig. 5 Error variation in a four-node quadrilateral element

5 Numerical assessment

Table 1 presents the six possibilities of element types that were implemented. In practice, it was observed that numerical results have shown to be mostly insensitive to the choice of element type. Elements C–F perform a little better compared to elements A–B in terms of convergence, i.e., they require fewer elements in the mesh in order to achieve accurate results. However, their quadratic and cubic global interpolation functions demand higher computational processing in order to numerically evaluate integrals along thickness. The conclusion is that the relatively better accuracy of elements C–F is offset by the numerical performance of elements A–B.

Regarding the local interpolation functions in Table 1, the linear/quadratic pair and the quadratic/cubic pair perform equally, at least in the simulations carried out in this work. Again, since cubic polynomials entail the necessity to use more integration points in the quadrature formulae, the pair linear/quadratic local functions is the preferred choice.

In light of these preliminary conclusions, element A (the simplest), both tria and quad topologies, are employed in the simulations. The mechanical properties used are those of a typical unidirectional ply of a UD [9]: $E_1 = 150.0$ GPa, $E_2 = E_3 = 10.0$ GPa, $G_{12} = G_{13} = 5.0$ GPa, $G_{23} = 3.378$ GPa, $\nu_{12} = \nu_{13} = 0.30$, $\nu_{23} = 0.48$; $\alpha_1 = 1.39 \times 10^{-7}$ K^{-1}, $\alpha_2 = \alpha_3 = 9.0 \times 10^{-6}$ K^{-1}. In the 0° layer, the principal directions (1, 2, 3) are aligned with the global axes (x, y, z).

5.1 A single laminate plate

In the first case, a square plate with edge lengths $a = b = 1$ m is investigated in detail. The laminate is chosen in the cross-ply [0°/90°], where the two layers have equal thicknesses. Thick and thin laminates are considered. In the thick laminate case, the total thickness is $h = 0.25$ m, and in thin laminate case, the total thickness is $h = 0.05$ m. A measure of the relative thinness of the laminates is given by the ratio $s = a/h$. Hence, the thick laminate has $s = 4$ and the thin laminate has $s = 20$. The boundary conditions assumed are illustrated in Fig. 6 and they are: $u(0, y, 0) = w(0, y, 0) = 0$, $u(a, y, 0) = w(a, y, 0) = 0$, $v(x, 0, 0) = w(x, 0, 0) = 0$ and $v(x, b, 0) = w(x, b, 0) = 0$. The plate is loaded on the top surface ($z = +h/2$) with $p_0 = \sigma_z = 100$ MPa, while the bottom surface ($z = -h/2$) is free.

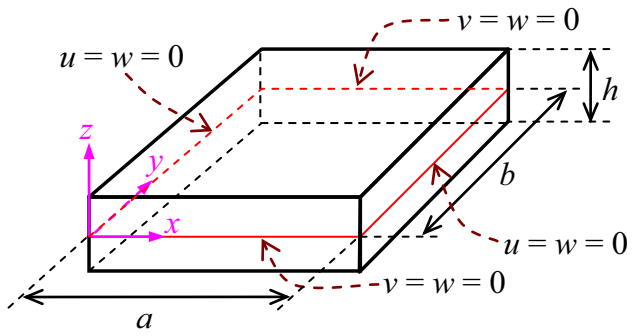

Fig. 6 Boundary conditions of single laminate plate

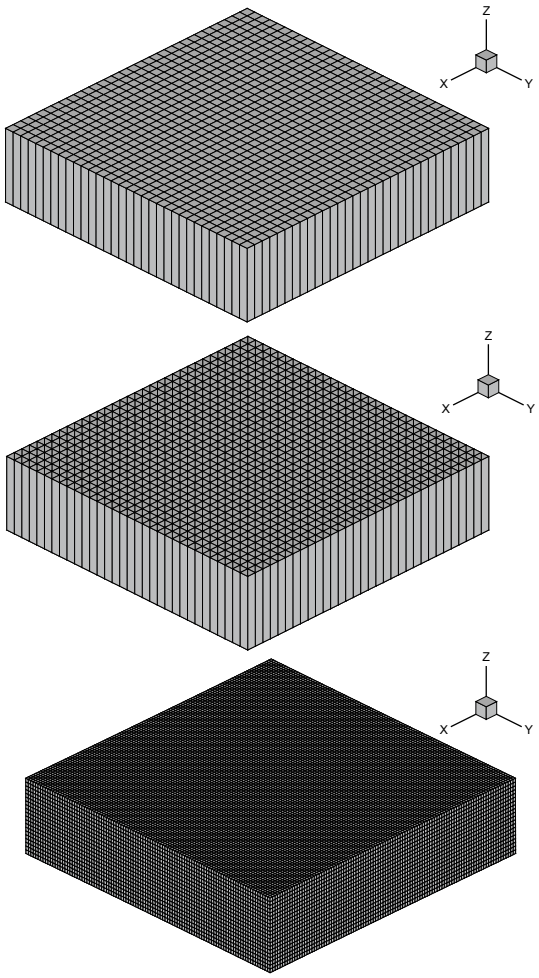

Fig. 7 Quad, tria and brick element meshes

Three models of the plate were considered: a 33×33 mesh of the new quad elements, a $2\times(33\times33)$ mesh of the new tria elements and a $100\times100\times20$ mesh of traditional eight-node brick elements. Both thick ($s=4$) and thin ($s=20$) laminate plates were modeled using the same meshes that can be seen in Fig. 7. The meshes shown in Fig. 7 were selected following a convergence analysis. A series of coarser meshes were tried before reaching the 33×33 mesh utilized. In the case of the tridimensional model, the problem lies in the imposition of the boundary conditions on the bottom and top surfaces. If too few 3D elements are used in the thickness direction, the enforced conditions $\sigma_z(-h/2)=0$, $\sigma_z(+h/2)=p_0$, $\tau_{xz}(\pm h/2)=0$ and $\tau_{yz}(\pm h/2)=0$ are not accurately satisfied. Hence, it was determined that 20 elements must be used in the z direction. The number of 3D elements in the x and y directions (100×100) follows from consideration of the aspect ratio.

The results are presented for displacement, strain and stress distributions along thickness. Distributions of w, ε_x, ε_y, ε_z, σ_x, σ_y, σ_z are shown at $x=a/2$, $y=b/2$, whereas distributions of u, v, γ_{yz}, γ_{xz}, γ_{xy}, τ_{yz}, τ_{xz}, τ_{xy} are shown at $x=a/4$, $y=b/4$. All results are normalized according to Eq. (53).

$$
\begin{aligned}
&u^* = \frac{100E_2}{p_0hs^3}w,\ v^* = \frac{100E_2}{p_0hs^3}w,\ w^* = \frac{100E_2}{p_0hs^4}w\\
&\varepsilon_x^* = \frac{1}{E_1}\varepsilon_x,\ \varepsilon_y^* = \frac{1}{E_1}\varepsilon_y,\ \varepsilon_z^* = \frac{E_2}{p_0s^2}\varepsilon_z\\
&\gamma_{yz}^* = \frac{E_3}{p_0s}\gamma_{yz},\ \gamma_{xz}^* = \frac{E_3}{p_0s}\gamma_{xz},\ \gamma_{xy}^* = \frac{E_3}{p_0s^2}\gamma_{xy}\\
&\sigma_x^* = \frac{1}{p_0s^2}\sigma_x,\ \sigma_y^* = \frac{1}{p_0s^2}\sigma_y,\ \sigma_z^* = \frac{1}{p_0}\sigma_z\\
&\tau_{yz}^* = \frac{1}{p_0s}\tau_{yz},\ \tau_{xz}^* = \frac{1}{p_0s}\tau_{xz},\ \tau_{xy}^* = \frac{1}{p_0s^2}\tau_{xy}
\end{aligned}
\tag{53}
$$

The results for the thick laminate ($s=4$) are grouped in Figs. 8, 9 and 10, whereas the results for the thin laminate ($s=20$) are grouped in Figs. 11, 12 and 13. Figures 8 and 11 show the normalized displacements u^*, v^* and w^*. Figures 9 and 12 show the normalized strains ε_x^*, ε_y^*, ε_z^*, γ_{yz}^*, γ_{xz}^*, γ_{xy}^*. Figures 10 and 13 show the normalized stresses σ_x^*, σ_y^*, σ_z^*, τ_{yz}^*, τ_{xz}^*, τ_{xy}^*. In Figs. 8, 9, 10, 11, 12 and 13, the z coordinate is normalized according to $z^*=z/h$ such that $-0.5\le z^*\le0.5$.

Judging by Figs. 8 and 11, it is fair to say that the displacements are in good agreement with the fine traditional brick element FE mesh results. Notice that the horizontal axes in the w^* distributions are shifted, i.e., $3.6\le w^*\le4.4$ for $s=4$ and $0.42\le w^*\le0.46$ for $s=20$. In Fig. 11, u^* and v^* are seen to be almost perfectly linear, what is expected as the laminate gets thinner. The result is more conservative since the traditional FE model in Nastran delivers a smaller w^*. Similar trends regarding the distribution of the w displacement were observed in a previous paper [10], where a possible explanation for such behavior is related to the choice of the local interpolation functions.

The ε_x^*, ε_y^*, ε_z^*, γ_{xz}^* strain results for $s=4$ and $s=20$ are acceptable. The trends, magnitudes and discontinuity jumps are all well captured by the new element, both its

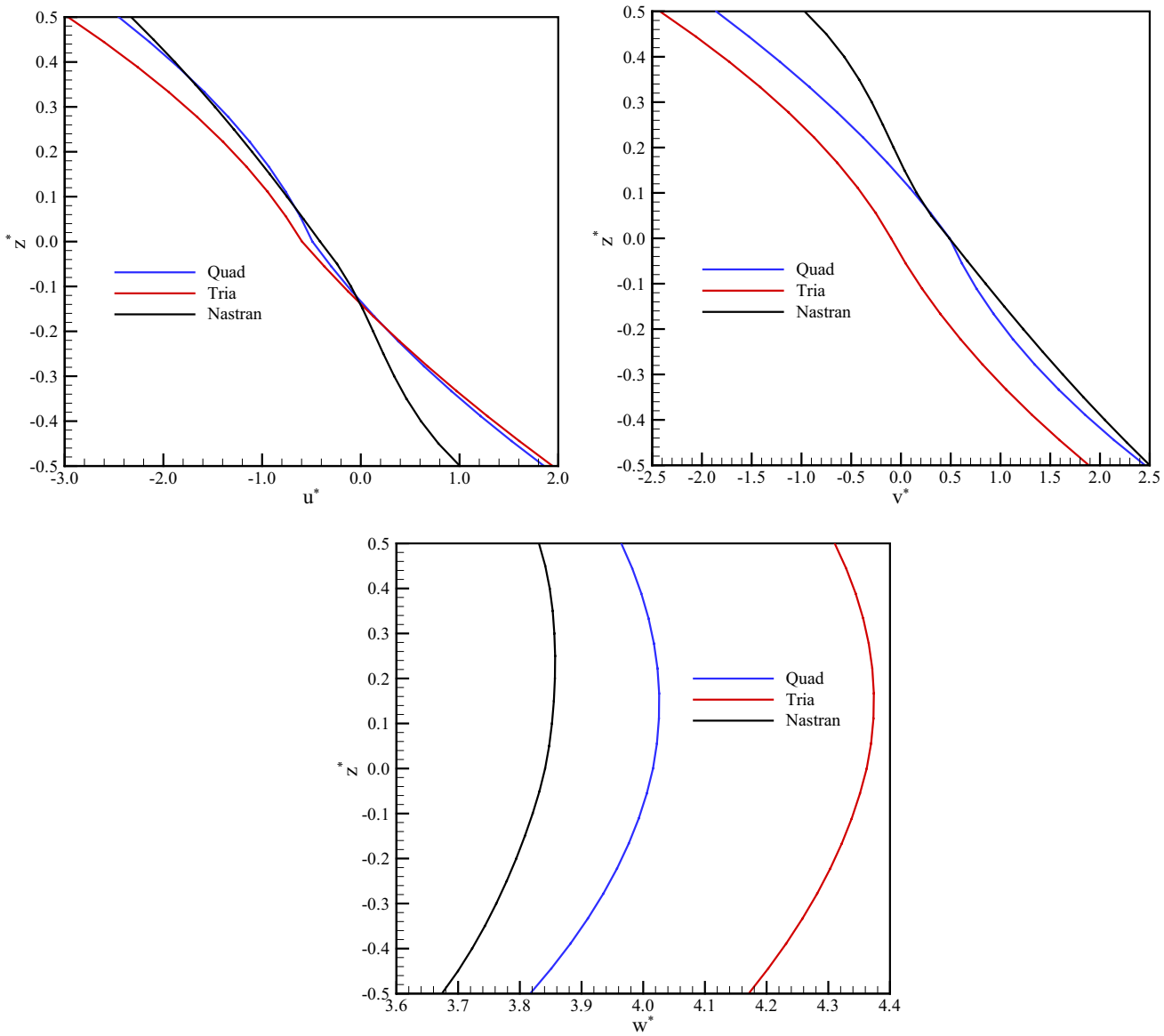

Fig. 8 Normalized displacement distributions along thickness for $s=4$. w^* is plotted at $x=a/2$ and $y=b/2$. u^* and v^* are plotted at $x=a/4$ and $y=b/4$

quad and tria versions. One very positive aspect of the new element is that the transverse normal strain ε_z^* computed is quite accurate. However, when it comes to γ_{xz}^*, γ_{xy}^* strains the results do not compare favorably against the traditional FE solution; particularly, γ_{xz}^* does not behave well, even presenting a discontinuity for the tria mesh case at $z^*=0$. A procedure to enhance accuracy of γ_{xz}^*, γ_{xy}^*, τ_{yz}^*, τ_{xz}^* can be achieved through post-processing of the results. The force equilibrium equations along x and y can be integrated through the thickness to yield Eq. (54). Once these improved transverse shear stresses are available, one can solve Eq. (4) to determine γ_{yz}, γ_{xz} as in $\tau_{yz}=C_{44}^{(k)}\gamma_{yz}+C_{45}^{(k)}\gamma_{xz}$ and $\tau_{xz}=C_{45}^{(k)}\gamma_{yz}+C_{55}^{(k)}\gamma_{xz}$.

$$\tau_{xz}=-\int_{-h/2}^{z}(\sigma_{x,x}+\tau_{xy,y})dz,\ \ \tau_{yz}=-\int_{-h/2}^{z}(\sigma_{y,y}+\tau_{xy,x})dz \tag{54}$$

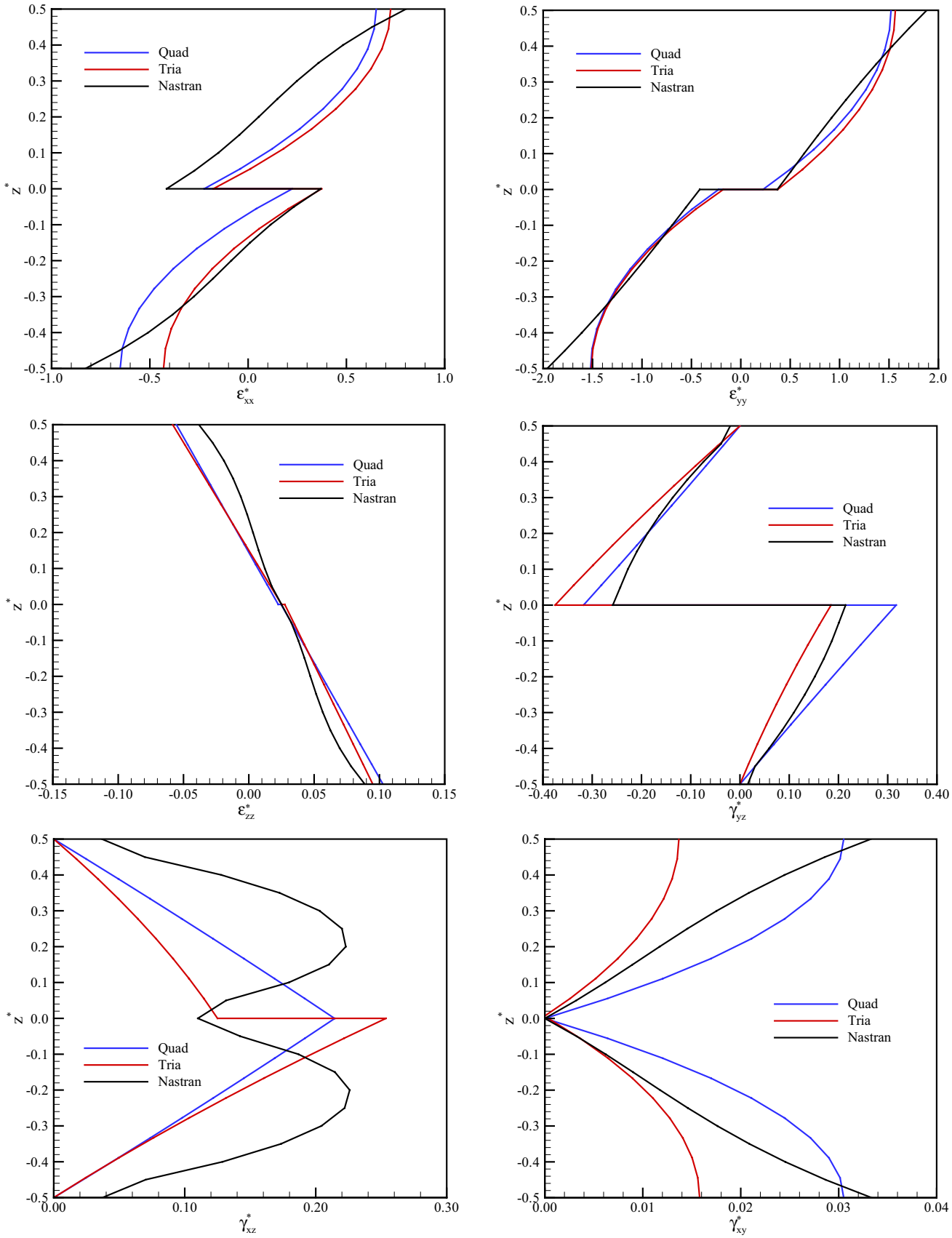

Fig. 9 Normalized strain distributions along thickness for $s=4$. ε_x^*, ε_y^*, ε_z^* are plotted at $x=a/2$ and $y=b/2$. γ_{yz}^*, γ_{xz}^*, γ_{xy}^* are plotted at $x=a/4$ and $y=b/4$

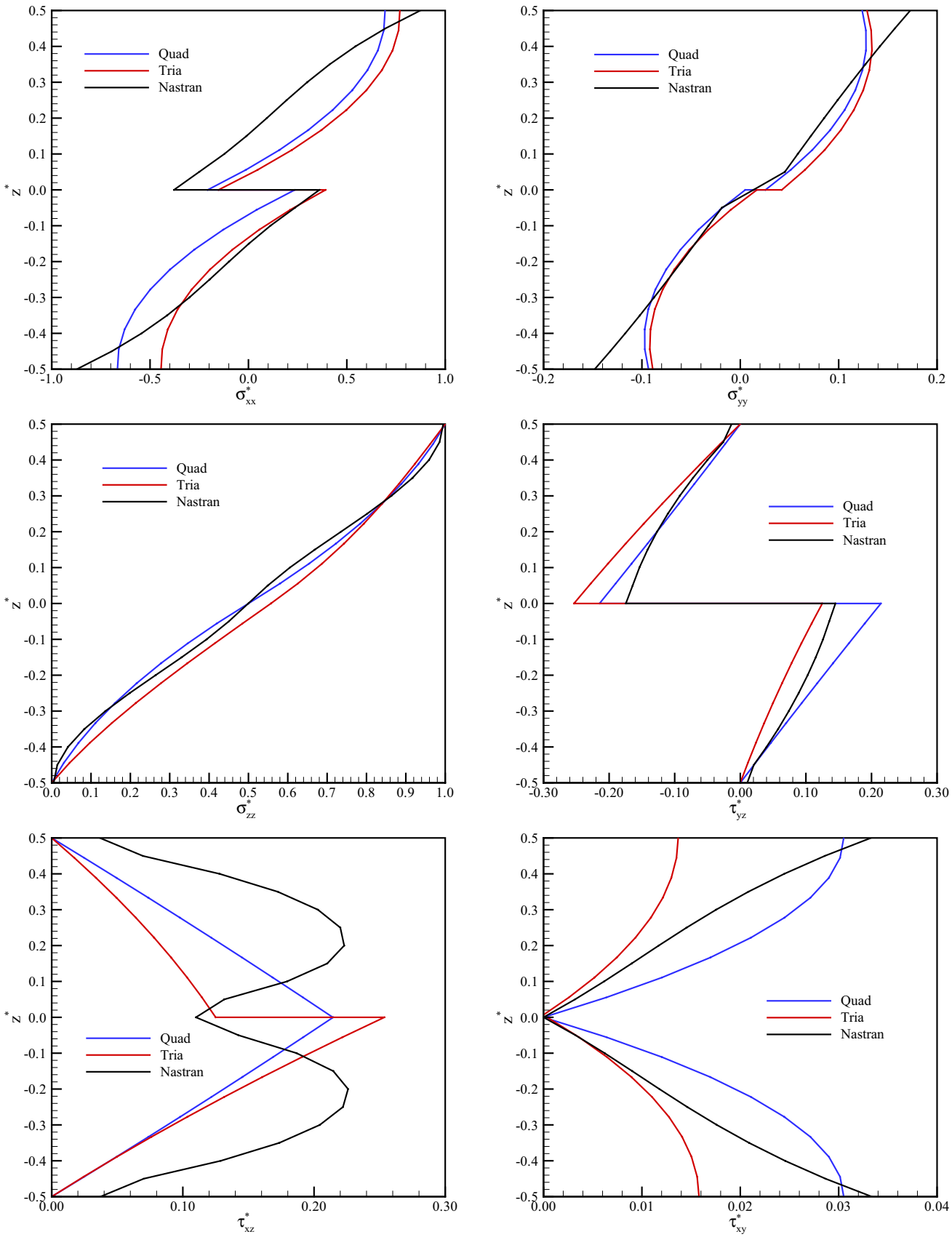

Fig. 10 Normalized stress distributions along thickness for $s=4$. σ_x^*, σ_y^*, σ_z^* are plotted at $x=a/2$ and $y=b/2$. τ_{yz}^*, τ_{xz}^*, τ_{xy}^* are plotted at $x=a/4$ and $y=b/4$

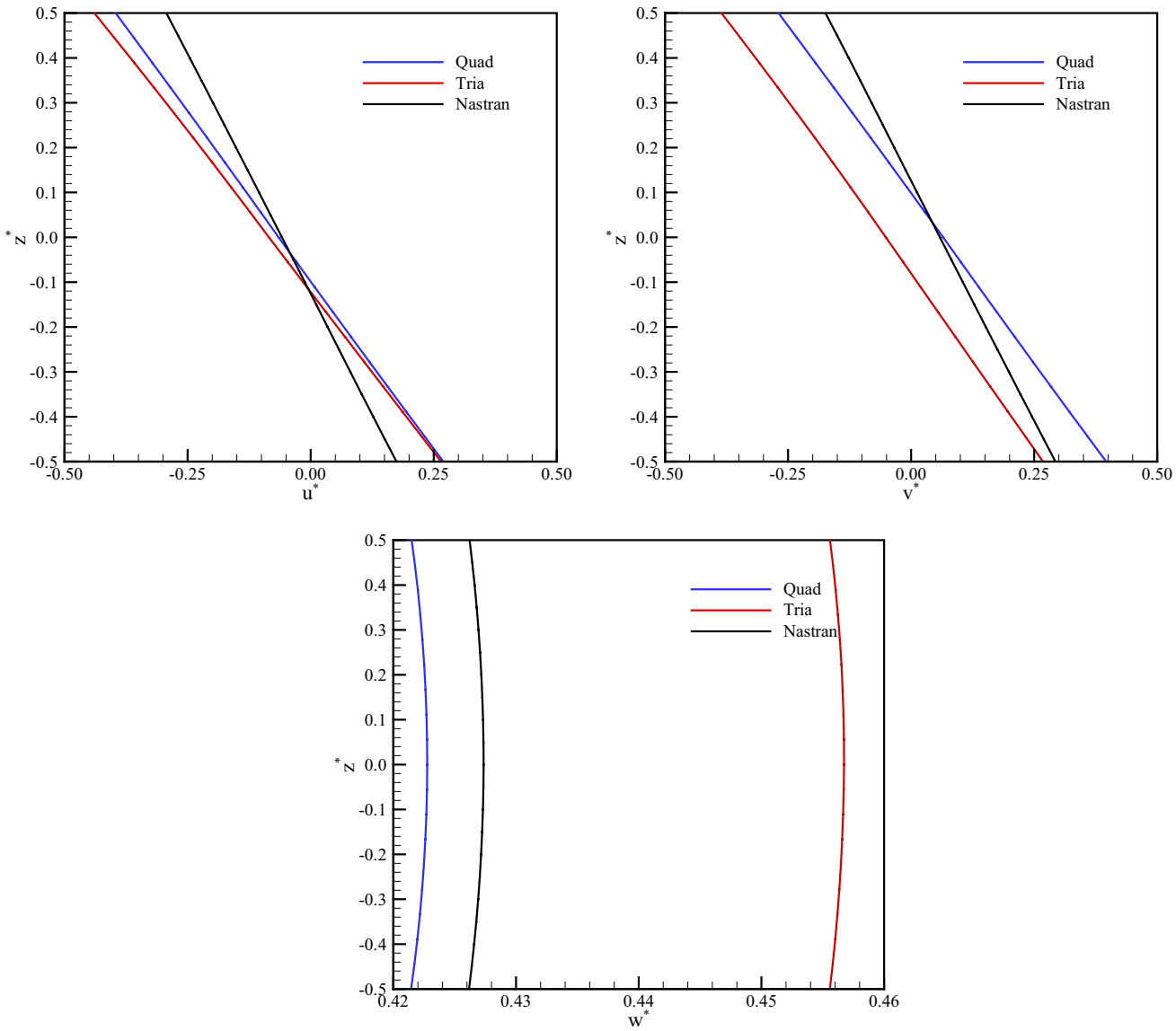

Fig. 11 Normalized displacement distributions along thickness for $s=20$. w^* is plotted at $x=a/2$ and $y=b/2$. u^* and v^* are plotted at $x=a/4$ and $y=b/4$

The tendencies of the strain results are carried on to the stresses. It is noticed that σ_x^*, σ_y^*, σ_z^*, τ_{xy}^*stress results are good, but τ_{yz}^*, τ_{xz}^* are not; particularly, τ_{xz}^* does not behave well. The good σ_z^* behavior is remarkable: It varies from 0 at the bottom surface up to 1 at the top surface, as expected. It is worth mentioning that the τ_{xz}^* obtained by Nastran is not zero at bottom ($z^*=-0.5$) and top ($z^*=0.5$) surfaces. This goes to show that even the fine mesh used by the commercial software is still incapable of predicting the correct answer $\tau_{xz}^*=0$. This is a quite alarming conclusion since, usually, solid FE models applied to laminate structures use only one or two solid elements per layer.

The traditional FE brick element mesh has 642,663 degrees of freedom, whereas the meshes used in partnership with the quad and tria elements have only 13,872 degrees of freedom, or almost 47 times less. This reflects in huge savings in the computational processing. Actually, it was observed that the factor of 47 times reflects directly in the processing time taken by the FE numerical solver, even recalling that the quadrature rule of numerical integration was used over each layer. The FE brick element mesh resulted in numerical models that required as much as 25× more processing time than the quad and tria meshes.

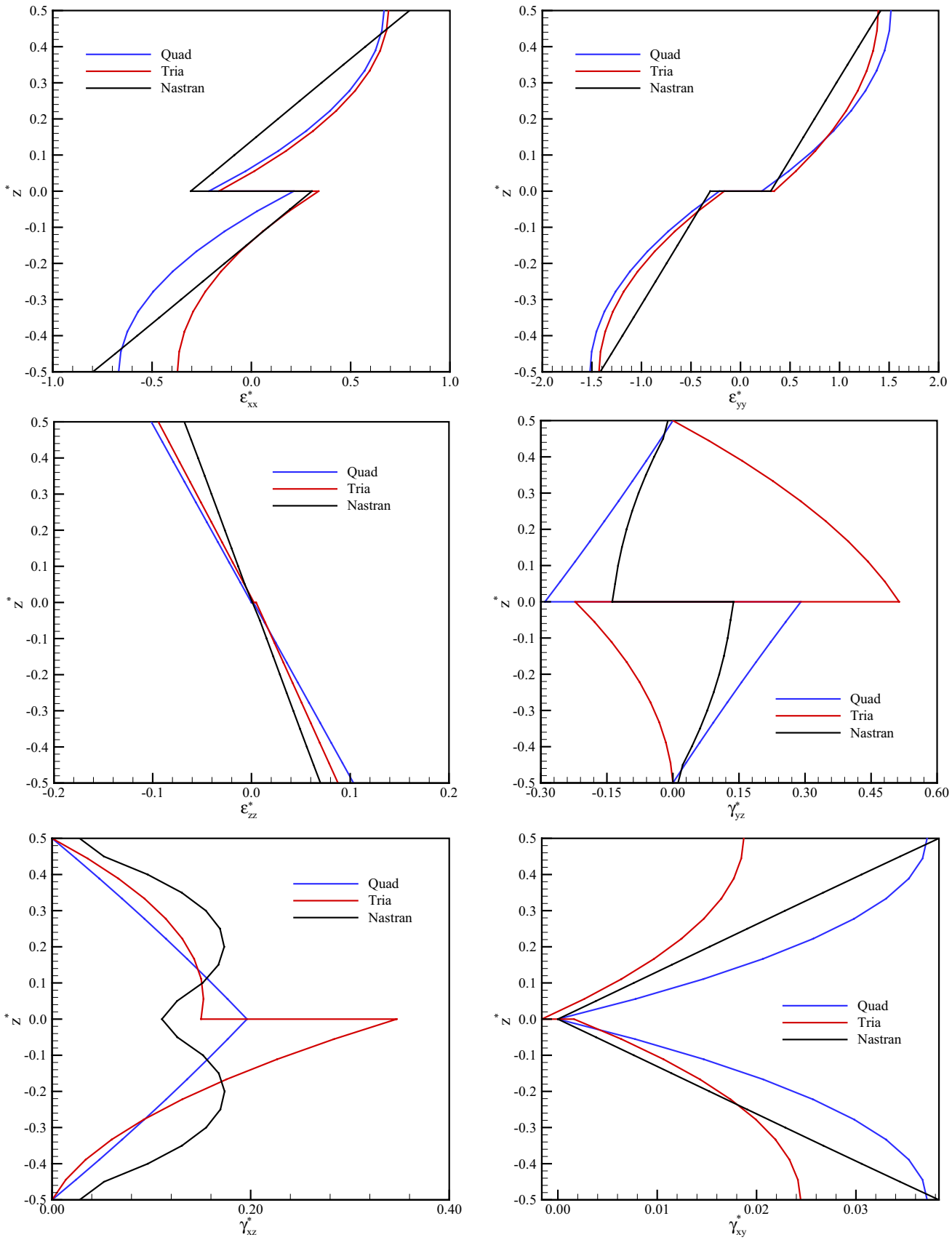

Fig. 12 Normalized strain distributions along thickness for $s=20$. ε_x^*, ε_y^*, ε_z^* are plotted at $x=a/2$ and $y=b/2$. γ_{yz}^*, γ_{xz}^*, γ_{xy}^* are plotted at $x=a/4$ and $y=b/4$

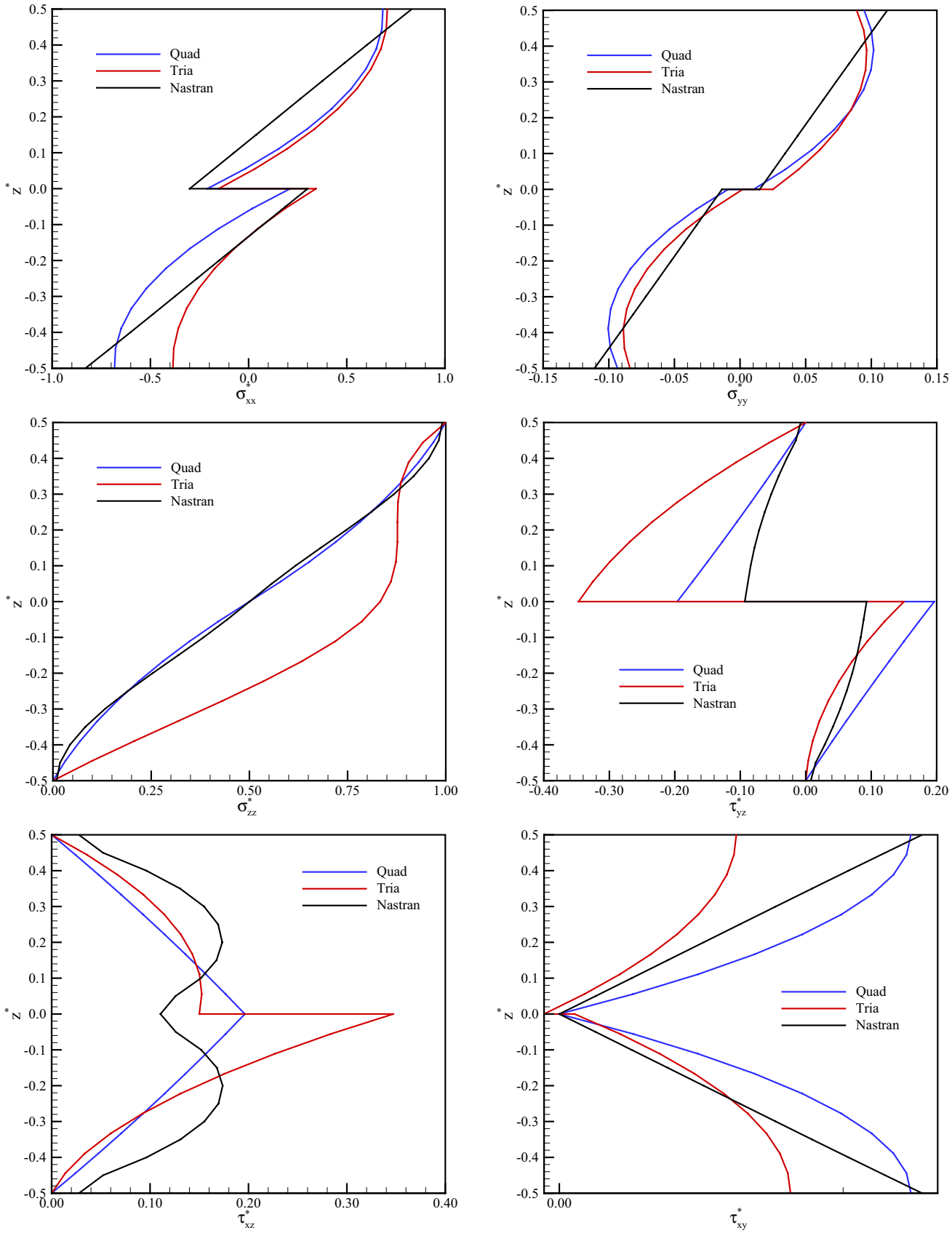

Fig. 13 Normalized stress distributions along thickness for $s=20$. σ_x^*, σ_y^*, σ_z^* are plotted at $x=a/2$ and $y=b/2$. τ_{yz}^*, τ_{xz}^*, τ_{xy}^* are plotted at $x=a/4$ and $y=b/4$

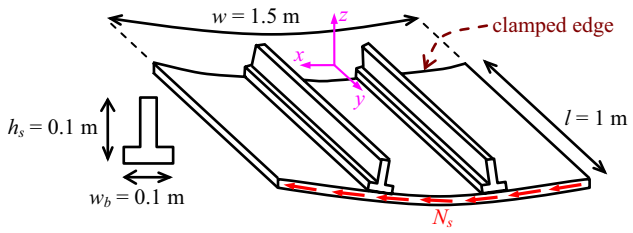

Fig. 14 Circular cylindrical stiffened composite panel

5.2 Stiffened panel

A more representative and practical composite structure is illustrated in Fig. 14 along with the dimensions chosen. A circular cylindrical panel with radius 5 m has two equally spaced reinforcements. One edge of the panel is clamped (no displacements and no rotations). The opposite edge is subject to a shear loading $N_s = 10$ kN/m that represents torsion.

The panel has multiple laminates whose material properties are the same as those used in the previous square

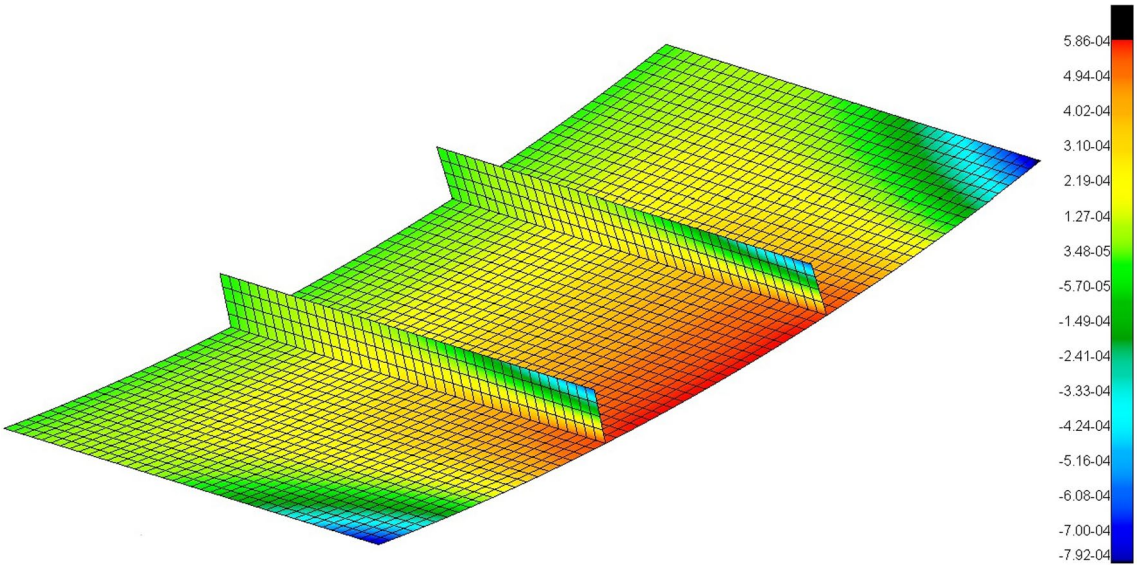

Fig. 15 Mindlin element mesh used to model the circular cylindrical stiffened composite panel. Result for the u displacement distribution

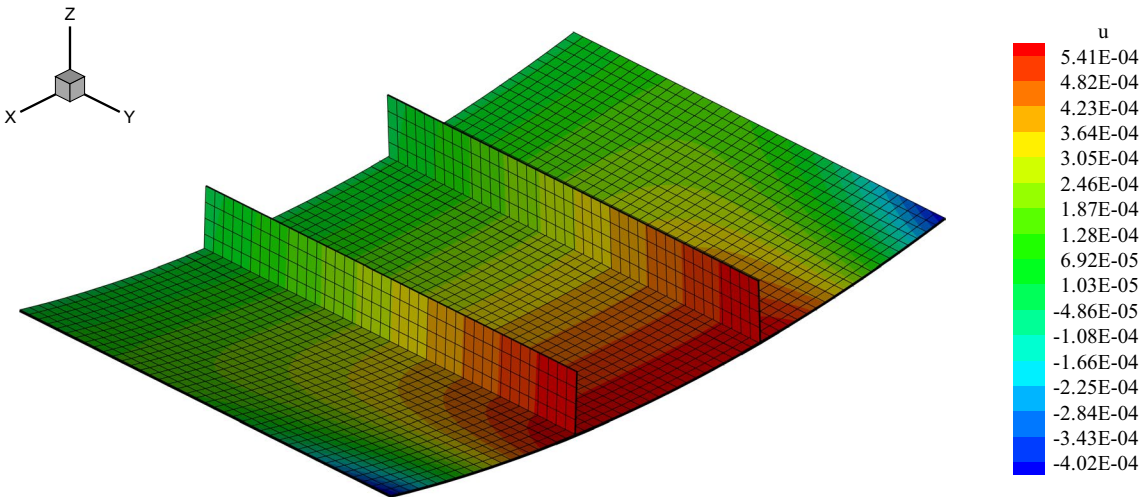

Fig. 16 Mesh of new elements used to model the circular cylindrical stiffened composite panel. Result for the u displacement distribution

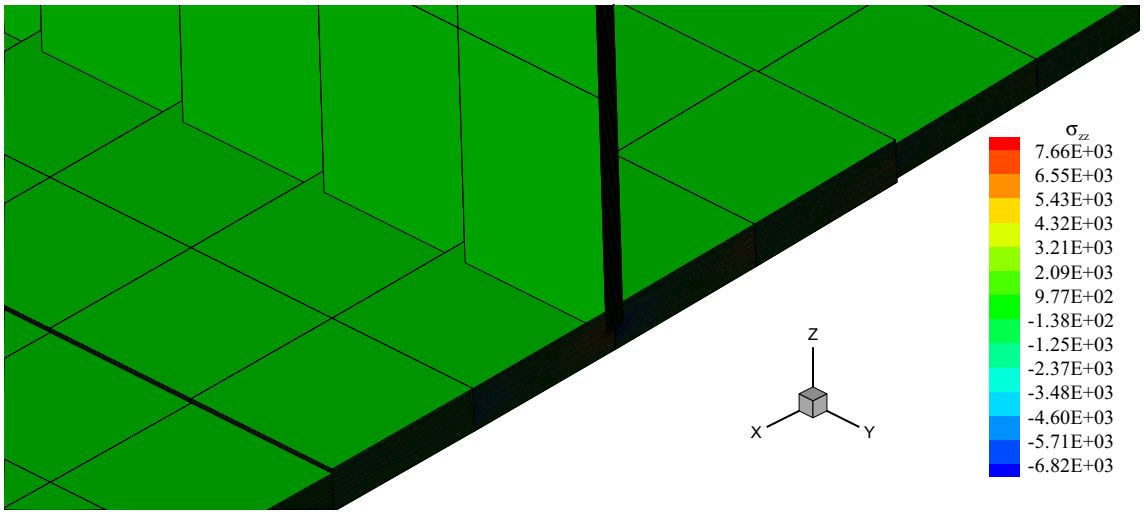

Fig. 17 Detail of the attachment region where stiffener and skin connect

plate example. Representing a more realistic application, each layer thickness is 0.15 mm. The layer orientations are defined according to y axis of Fig. 14, i.e., 0° ply angle means that the fibers are parallel to the y axis. The panel skin laminate is the $[0°/90°]_{6S}$ with a total of 24 layers. The reinforcement base laminate is the $[90°/0°]_3$ laminate with 6 layers in total. The reinforcement web is the $[0°/90°]_{5S}$ with a total of 20 layers. Notice that in the region where the stiffener base attaches to the panel skin the resulting laminate has 30 layers: $[[0°/90°]_{6S}, [90°/0°]_3]$.

Two models for this panel are simulated. The first model is composed of traditional four-node plate laminate elements based on Mindlin formulation. Sixty elements are used in the hoop direction (x axis), 40 elements are used in the longitudinal direction (y axis) and 4 elements are used along the stiffener height (z axis). Four elements are used to model the base of each stiffener. In the second model, the same mesh is used, but the new element formulated is employed.

Figures 15 and 16 show the results is terms of u displacement along x axis. The negative displacements (blue hue) observed in the Mindlin mesh on the region near the free tip of the stiffeners were not observed in the new element model. However, the displacement distribution over most of the reinforced panel agrees very well. The greatest advantage of the model built with the newly proposed element is its ability to assess through-the-thickness effects. Evidently, the Mindlin elements cannot predict neither ε_z nor σ_z and may provide inaccurate results in terms of γ_{yz}, γ_{xz}, τ_{yz}, τ_{xz}. Figure 17 shows a magnified view of the skin/stiffener attachment region. The laminate representing the connection skin/stiffener base with a total of 30 layers is clearly seen. Additionally, the transverse normal stress σ_z distribution is captured. This information is invaluable if studies toward stiffeners detachment are to be done.

6 Conclusions

Two versions of a new element are proposed (quad and tria). Their numerical implementations were described and performance assessment conducted. The element results compare well against a commercial FE package that used traditional eight-node brick elements to build a 3D model. Displacement, strain and stress magnitude, tendencies and discontinuities were reasonably well predicted. The quad element is superior to the tria, what is expected. It is good practice to use as many quads as possible and recur to a few trias only to avoid severe mesh distortions.

One important feature of the new element is that it can take advantage of previously existing meshes originally created to work with traditional quads and trias formulated under Mindlin hypothesis and build on them through-the-thickness capabilities. This is because the new element requires only that the parent tria or quad nodal positions are available, and from there, the element matrices and vectors can be computed without the need to create specially purposed 3D meshes.

Another great feature of the element is its ability to model multiple laminate structures such as the reinforced panel considered. In the simulations performed, the Mindlin element mesh presented in Fig. 15 was taken as the starting point for the model created using the new elements and depicted in Fig. 16. Figure 17 shows that the through-the-thickness capabilities of the new element allow one to

compute, for instance, σ_z, τ_{yz} and τ_{xz} stresses and 3D displacements, which can subsequently be used in conjunction with composite failure criteria [11] in the investigation of challenging phenomena involving crack propagation [12].

Funding Partial financial support was received from agencies CNPq (Grant 310742/2020–0) and FAPESP (Grant 2019/00917-8).

Declaration

Conflict of interest The author has no competing interests to declare that are relevant to the content of this article.

References

1. Carrera E (1997) CZ0 requirements-models for the two dimensional analysis of multilayered structures. Compos Struct 37(3–4):373–383. https://doi.org/10.1016/S0263-8223(98)80005-6
2. Li X, Liu D (1995) A laminate theory based on global–local superposition. Commun Numer Methods Eng 11(8):633–641. https://doi.org/10.1002/cnm.1640110802
3. Carrera E (2003) Theories and finite elements for multilayered plates and shells: a unified compact formulation with numerical assessment and benchmarking. Arch Comput Methods Eng 10(3):215–296. https://doi.org/10.1007/BF02736224
4. Liu D, Li X (1996) An overall view of laminate theories based on displacement hypothesis. J Compos Mater 30(14):1539–1561. https://doi.org/10.1177/002199839603001402
5. Hughes TJR (1987) The finite element method: linear static and dynamic finite element analysis, 1st edn. Prentice-Hall, Englewood Cliffs
6. Cowper GR (1973) Gaussian quadrature formulas for triangles. Int J Numer Meth Eng 7(3):405–408. https://doi.org/10.1002/nme.1620070316
7. Allman DJ (1984) A compatible triangular element including vertex rotations for plane elasticity analysis. Comput Struct 19(1–2):1–8. https://doi.org/10.1016/0045-7949(84)90197-4
8. Ibrahimbegovic A, Taylor RL, Wilson EL (1990) A robust quadrilateral membrane finite element with drilling degrees of freedom. Int J Numer Meth Eng 30(3):445–457. https://doi.org/10.1002/nme.1620300305
9. Rolfes R, Noor AK, Sparr H (1998) Evaluation of transverse thermal stresses in composite plates based on first-order shear deformation theory. Comput Methods Appl Mech Eng 167(3–4):355–368. https://doi.org/10.1016/S0045-7825(98)00150-9
10. Lima AS, de Faria AR. A unified formulation for composite quasi-2D finite elements based on global-local superposition. *Composite Structures*, **254**: article ID 112846, 2020. https://doi.org/10.1016/j.compstruct.2020.112846
11. Donadon MV, Almeida SFM, Arbelo MA, de Faria AR (2009) A three-dimensional ply failure model for composite structures. Int J Aerospace Eng. Article ID 486063. https://doi.org/10.1155/2009/486063
12. Bürger D, de Faria AR, Almeida SFM, Melo FCL, Donadon MV (2012) Ballistic impact simulation of an armour-piercing projectile on hybrid ceramic/fiber reinforced composite armours. Int J Impact Eng 43:63–77. https://doi.org/10.1016/j.ijimpeng.2011.12.001